Noncollinear and collinear magnetic structures in exchange coupled Fe/Cr(001) superlattices

A. Schreyer
Experimentalphysik/Festkörperphysik, Ruhr-Universität Bochum, D-44780 Bochum, Germany

J. F. Ankner
Missouri University Research Reactor, Columbia, Missouri 65211

Th. Zeidler and H. Zabel
Experimentalphysik/Festkörperphysik, Ruhr-Universität Bochum, D-44780 Bochum, Germany

M. Schäfer, J. A. Wolf,* and P. Grünberg
Forschungszentrum Jülich, D-52425 Jülich, Germany

C. F. Majkrzak
National Institute of Standards and Technology, Gaithersburg, Maryland 20899
(Received 28 April 1995 revised manuscript received 7 September 1995)

The magnetic and structural properties of molecular beam epitaxy grown Fe/Cr(001) superlattices were studied as a function of the growth temperature T_g using polarized neutron reflectometry (PNR) with polarization analysis, magneto-optic Kerr effect (MOKE), and x-ray-scattering techniques. From MOKE and PNR as a function of external field we find strong noncollinear coupling between the Fe layers and a so far unexpected coupling angle of 50° near remanence for a sample grown at $T_g = 250$ °C. A detailed discussion of the domain structure of the sample near remanence confirms the modeling. On the other hand, an otherwise equivalent sample grown at room temperature exhibits completely ferromagnetic or uncoupled behavior. Using diffuse x-ray-scattering methods these distinct differences in the magnetic structure are found to be correlated with a growth temperature dependent length scale of constant Cr interlayer thickness l_{Cr}. We find that l_{Cr} increases significantly with T_g. These results are discussed in the framework of current theories of noncollinear exchange. It is demonstrated that the bilinear-biquadratic formalism used so far is inconsistent with the data. The Cr specific proximity magnetism model is discussed which explains the occurrence of noncollinear coupling for systems with Cr interlayer thickness fluctuations on the length scale observed here for $T_g = 250$ °C. The model yields an exchange energy different from the bilinear-biquadratic formalism used so far, explaining the asymptotic approach to saturation observed by MOKE.

I. INTRODUCTION

A. Oscillatory exchange coupling

In the past decade, improved sample preparation techniques have made it possible to study magnetic thin film systems of unprecedented quality, revealing new physical properties. Among these findings was that of the oscillatory exchange coupling between ferromagnetic (FM) layers. Starting in 1986, various groups around the world discovered that in such systems an interlayer thickness dependent magnetic exchange coupling between ferromagnetic layers can be mediated by a non-FM interlayer. This coupling was found to be oscillatory with interlayer thickness between antiferromagnetic (AF) and FM with oscillation periods, which depend on the interlayer material. This discovery was made independently for rare earth (RE) (Ref. 1) and transition metal (TM) systems.

Among the TM systems Fe/Cr(001) has played an extremely important role. It was the first TM system which was found to exhibit AF exchange coupling.[2] The "giant magnetoresistance" (GMR), which can be a consequence of the AF coupling, was also found in Fe/Cr.[3,4] Using this effect, evidence for the oscillatory nature of the exchange coupling was found for Fe/Cr, Co/Cr, and Co/Ru.[5] Subsequently it was demonstrated, e.g., by a combined Brillouin light scattering (BLS) and magneto-optic Kerr effect (MOKE) study of the Fe/Cr system, that at intermediate spacer thicknesses between the AF coupled regions the coupling actually is FM in nature.[6] Since then in a large number of $3d$, $4d$, and $5d$ TM systems evidence for oscillatory exchange coupling has been found (see, for example, Ref. 7). For a recent review of the properties of thin magnetic TM films see, e.g., Refs. 8 and 9.

Whereas the oscillatory exchange coupling was quickly explained for the case of the RE systems,[1,10] the exchange mechanism for the TM structures initially was not so well understood. Only by taking into account the topological properties of the Fermi surface of the interlayer and its discrete atomic structure could the coupling properties be explained by Bruno and Chappert,[11] Edwards *et al.*,[12] and Coehoorn,[13] among others. Within a Ruderman-Kittel-Kasuya-Yosida (RKKY) approach, Bruno and Chappert[11,14] correlated the oscillatory exchange coupling with vectors which connect parts of the Fermi surface of the interlayer with antiparallel Fermi velocities. These vectors $\vec{q}$ are parallel to the growth direction of the interlayer. The oscillation period L of the coupling is then given by $|\vec{q}| = 2\pi/L$. It

immediately follows from the topology of the Fermi surface that in general the period and the number of possible oscillations sensitively depend on the growth direction of the magnetic thin film system. These theoretical predictions have been confirmed, e.g., in the model system Co/Cu for the (001),[15] (110),[16] and (111) (Ref. 17) growth orientations. Although the theory of Bruno and Chappert is physically transparent and has been successful in the prediction of exchange coupling properties it does not yet correctly describe the strength and phase of the coupling oscillations.[14] Many other theoretical approaches and models have been proposed,[18–20] but significant discrepancies between theory and experiment remain.

Since real samples will not have perfectly flat interfaces, the influence of roughness must also be taken into account. It has been suggested[21] that interface roughness is the reason why theories usually overestimate the coupling strength. Roughness induces varying effective layer thicknesses, whose phases interfere destructively reducing the total coupling strength. Wang *et al.*[22] demonstrated for the case of Fe/Cr(001) that roughness can even suppress an otherwise predicted short period oscillation period of two monolayers. This effect has been confirmed more generally by Bruno and Chappert.[14] They showed that short period oscillations are more sensitive to roughness than long period ones, i.e., roughness acts as a low-pass filter for the oscillation frequency. Furthermore, they demonstrated that the angle between the sample's growth direction and the Fermi velocity of those electrons which mediate the coupling is an additional significant parameter for the sensitivity to interface roughness. Nonetheless, as detailed below, roughness may have additional effects which can qualitatively modify the nature of the coupling.

B. Noncollinear exchange coupling

In 1991, again in Fe/Cr, Rührig *et al.* reported that in the transition regions of the coupling constant J between *collinear* 180° (AF) and 0° (FM) spin alignment, a *noncollinear* 90° coupled magnetization profile exists.[23] These findings were made on molecular-beam epitaxy (MBE) grown epitaxial Fe/Cr/Fe(001) trilayers with a wedge shaped Cr interlayer which provided a large range of Cr thicknesses in one sample. The magnetic structure was deduced from Kerr microscopy and MOKE hysteresis curves. Similar results were obtained at about the same time by Heinrich *et al.* on Co/Cu/Co(001) trilayers using MOKE.[24]

In a phenomenological approach, Rührig *et al.* rationalized their finding by postulating the existence of an additional *biquadratic* exchange coupling term J^{BQ},[23] which can favor a 90° spin alignment. The exchange coupling energy per unit area can then be written

$$E(\varphi) = -J^{BL}\hat{m}_1 * \hat{m}_2 - J^{BQ}(\hat{m}_1 * \hat{m}_2)^2, \qquad (1)$$

where J^{BL} is the usual *bilinear* Heisenberg term describing the oscillatory exchange coupling. $\hat{m}_1$ and $\hat{m}_2$ are unit vectors parallel to the magnetizations of the two neighboring layers 1 and 2 and φ_c is the angle between $\hat{m}_1$ and $\hat{m}_2$, which results from minimization of Eq. (1). The oscillatory exchange coupling between AF and FM then simply is described by an oscillation of J^{BL} between positive and negative values with $J^{BQ}=0$. If J^{BL} and J^{BQ} are both negative and $|J^{BL}|>|J^{BQ}|$, Eq. (1) has a minimum for an AF magnetization profile ($\varphi_c=180°$) whereas for $|J^{BL}|<|J^{BQ}|$ the minimum occurs for a noncollinear spin structure with ($\varphi_c=90°$). A positive J^{BL} causes FM coupling whereas a positive J^{BQ} produces minima for FM and AF magnetization profiles. Thus a large negative J^{BQ} is required to induce any noncollinear spin structure. This bilinear-biquadratic formalism for exchange coupling is widely used nowadays. It is equivalent to the one which Heinrich *et al.*[24] introduced to explain their MOKE data.

In the meantime, evidence for the significance of the biquadratic term has been found by various groups on a number of systems (see, e.g., Refs. 25–31 and the list of references in Ref. 32). Furthermore, a number of physical mechanisms have been proposed for the origin of the biquadratic term.

1. Fluctuation mechanism

A theoretical explanation was suggested by Slonczewski,[33] who proposed that the biquadratic coupling is a *secondary* effect, which can simply result from a terraced interlayer thickness variation on a lateral length scale l in the sample plane. He showed that such a lateral thickness variation by one monolayer can lead to a biquadratic contribution, e.g., in transition spacer thicknesses between $J^{BL}<0$ and $J^{BL}>0$, where $J^{BL}\approx 0$. Here, a monolayer thickness variation can induce a fluctuation $2\Delta J^{BL}$ between AF ($J^{BL}<0$) and FM ($J^{BL}>0$) coupling. Such a fluctuation is especially strong in the case of an additional inherent two monolayer oscillation period of J^{BL}. This short oscillation period had been predicted for Fe/Cr(001) theoretically for the case of small interface roughnesses.[22] It was subsequently discovered experimentally.[34,35,6] Since the exchange stiffness caused by the FM coupling *within* the FM layer wants to prevent such an interlayer thickness-induced variation between AF and FM magnetization profiles, an intermediate coupling angle results. From minimization of the sum of the exchange coupling energy and the intralayer FM stiffness energy, a coupling angle of 90° is obtained. Paradoxically, J^{BQ} increases with l, as the specimen becomes more nearly perfect, up to the point $J^{BQ}\simeq\Delta J^{BL}$, where the theory breaks down. Only for very large lateral length scales l of this interlayer thickness fluctuation (i.e., larger than typical domain wall sizes) can FM and AF domains form in the system. The theory was found to be consistent with the data of Rührig *et al.* [23] and with images obtained by scanning electron microscopy with polarization analysis (SEMPA) on Fe/Cr/Fe(001) and Fe/Ag/Fe(001) trilayers.[34,28,31] It was also confirmed by experiments and detailed analysis for Fe/Cu/Fe trilayers.[26] Furthermore, numerical investigations by Ribas and Dieny confirmed the significance of this so-called *fluctuation mechanism*.[36,37]

2. Other mechanisms for biquadratic coupling

Whereas the fluctuation mechanism is a structurally induced effect of the bilinear term it has been shown that a biquadratic contribution also may arise *intrinsically* as a second-order term from the electronic structure of an interlayer with ideal interfaces.[18,38–41] As, for example, the case

of Fe/Al/Fe (Ref. 25) shows, the intrinsic mechanism usually is, however, too weak to account for the observed biquadratic term alone.[41,42] Furthermore, the intrinsic mechanism can also be ruled out as the governing effect since it predicts an oscillation of J^{BQ} around zero whereas $J^{BQ}<0$ has always been found experimentally so far.

Subsequently, Slonczewski proposed the *loose spin* mechanism.[32] He postulated the existence of localized electron states with unpaired spins located within or at the interfaces of an otherwise nonmagnetic metallic spacer layer. Loose exchange coupling of these spins to the two adjacent FM layers mediates a non-Heisenberg exchange coupling between them which includes a biquadratic term $J^{BQ}<0$ for all spacer thicknesses. A similar model was proposed at about the same time by Barnaś and Grünberg.[39] Slonczewski's model turned out to be consistent with the sign and temperature dependence of the biquadratic term measured for Fe/Al/Fe (Ref. 29) and Fe/Au/Fe (Ref. 43) trilayers.[32] Furthermore, the significance of this mechanism has recently been confirmed by Schäfer *et al.*[44] and Heinrich *et al.*[45] who deliberately introduced loose spins into the nonmagnetic interlayer. However, the loose spin mechanism is much too weak to explain the strong biquadratic coupling reported for Fe/Cr. This conclusion can be drawn from the data of Schäfer *et al.*[44] on the Fe/Ag system, since no drastic changes in any of the parameters relevant for the theory are expected from interchanging Ag and Cr.

Another mechanism takes into account the magnetic dipole field of magnetic layers with interface roughness.[46] Computer simulations and estimates show that this mechanism can provide a coupling strength on the order of the one found for Fe/Au/Fe.[25] Nevertheless, this mechanism by itself cannot explain the strength of the biquadratic coupling found in Fe/Cr.[46]

3. *Proximity magnetism model*

Most recently Slonczewski has suggested a phenomenological model for noncollinear coupling which is based on the intrinsic AF structure of Cr (or Mn) and a long-range lateral interlayer Cr (Mn) thickness fluctuation of length scale l.[47] The model is based on the assumption that the adjoining ferromagnets polarize the Cr interlayer leading to an AF structure also above its bulk Néel temperature $T_N^{b,Cr}$ (proximity magnetism). Experimental support for this assumption comes from the SEMPA studies by Unguris *et al.*,[34,48] who reported the persistence of the spin density wave magnetism of Cr well above $T_N^{b,Cr}$.

Slonczewski proposes the existence of helicoidally twisted quasi-antiferromagnetic proximity states in the Cr (Mn) which lead him to a coupling energy completely different from the conventional one used so far [Eq. (1)]. The exchange coupling energy per unit area can then be written

$$E(\varphi)=J_+\left(\frac{\varphi}{\pi}\right)^2+J_-\left(\frac{\pi-\varphi}{\pi}\right)^2, \qquad (2)$$

with $J_{+,-}\geq 0$ and $0\leq\varphi\leq\pi$. For $J_+>0$, $J_-=0$ ($J_+=0$, $J_->0$), Eq. (2) has minima for FM (AF) alignment, whereas noncollinear structures are obtained for $J_+>0$ and $J_->0$. For a *perfect* sample with an integer number of monolayers in the spacer either one or the other coefficient will vanish since the coupling is thought to be determined by the internal two monolayer period AF structure of the Cr. An interlayer thickness fluctuation therefore induces contributions from both coefficients which, due to the internal FM stiffness of the FM layers, results in a noncollinear spin structure. Similar to earlier findings for Slonczewski's first interlayer fluctuation based model,[33] it appears plausible that this mechanism will also be negligible for very small l. In this case, locally, the number of interlayers will not be sufficiently well defined. However, Slonczewski also shows that the proximity magnetism model only works for $l\leq 100$ Å.[48]

C. The situation in Fe/Cr(001)

Although Fe/Cr(001) has been one of the most heavily studied systems in the field of exchange coupled thin films, its properties are not yet fully understood. In the present paper we, on one hand, help resolve open questions and, on the other hand, present surprising results.

From the above discussion it is evident that the structure of the sample can have a significant influence on the coupling properties. This is confirmed by data published on the system Fe/Cr(001) by various groups. The initially observed long period oscillation is found for growth at RT,[6,34,49,31] whereas at an elevated growth temperature of 250–300 °C an additional two monolayer oscillation is observed. This oscillation is generally attributed to the nesting vector $\vec{q}_s^{Cr}$ of Cr which also gives rise to the well known spin density wave antiferromagnetism in bulk Cr. Furthermore, the biquadratic coupling component was found to increase significantly with growth temperature.[49]

However, considerable disagreement remains for many details of the data which, in part, could be explained by the fact that different substrates with different surface roughnesses have been used. For example, for growth on GaAs substrates around 300 °C the biquadratic contribution is found to be much larger[49] than for samples grown on Fe whiskers,[8,31] which are expected to exhibit a much flatter surface. Nevertheless, even for growth on Fe whiskers the origin of the observed biquadratic coupling (e.g., the role of Slonczewski's fluctuation mechanism) is not well understood.[8,31]

In the present paper, we will demonstrate that the detailed structure of the interfaces is the key to the understanding of the growth temperature induced changes in the magnetic properties of the Fe/Cr system. So far this problem has only been investigated using *surface* science methods,[8,31] which yield no information on *internal* interfaces. We show how the relevant information on internal interfaces and layer thickness variations can be extracted from small angle x-ray data in a simple nondestructive way. Alternatively, it has been suggested[50] that the crystalline quality might be different in samples grown at RT and at 250 °C, thus inducing the observed growth temperature dependence of the magnetic properties. Here, we present an extensive x-ray study of the effect of the growth temperature on the interfaces and the crystalline structure of the Fe/Cr(001) system.

A large body of neutron work exists by now on the well accepted AF spin structure in Fe/Cr for certain layer thicknesses[51–54] and its correlation with the giant magnetoresistance effect.[55–59] In contrast, hardly any neutron studies of

transition metal systems exhibiting noncollinear spin structures are available up to now. In particular, no such data exist for the important system Fe/Cr(001), apart from our own results.[60–62] Neutron scattering is a powerful method for determining the magnetic structure on a microscopic scale, including the magnitude of the magnetic moments and their orientation. The distinction between collinear and noncollinear spin structures poses a challenge since both structures double the magnetic over the nuclear superlattice periodicity causing magnetic half-order peaks. A method ideally suited for this task therefore is polarized neutron reflectivity (PNR) with exit beam polarization analysis. It allows for the determination of the magnitude as well as the orientation of the magnetic moments in the film plane (see Ref. 63 for a comparative review of PNR from collinear and noncollinear magnetization profiles).

In this paper PNR and MOKE data are presented which make possible detailed conclusions about the coupling angle and the strength of the exchange coupling as a function of the growth temperature. For growth at 250 °C we find a coupling angle of 50° near remanence instead of the perpendicular alignment reported so far. We demonstrate the drastic influence of the growth temperature on the magnetic properties of the system and correlate these findings with our x-ray results providing strong evidence for the proximity magnetism model.

The remainder of the paper is organized as follows: After a brief overview of the experimental methods we give a detailed account of the structural characterization of the samples grown at RT and 250 °C. Then the PNR measurements near remanence on the noncollinearly coupled samples grown at 250 °C are described, including a thorough discussion of the possible influence of magnetic domains on the scattering. Subsequently the field dependent PNR and MOKE data are presented and compared with data of an equivalent sample grown at RT. In the final section we rationalize all our findings presenting strong evidence for proximity magnetism in Fe/Cr.

II. EXPERIMENTAL METHODS

A. Sample preparation

The samples used in this study were grown by Schäfer, Wolf, and Schreiber of Grünberg's group in Jülich by MBE methods on the same GaAs/Fe/Ag substrate-buffer system described in Refs. 23 , 49, and 50. First, a 10 Å thick Fe seed layer was deposited on the GaAs(001) substrate, followed by a 1500 Å Ag buffer, providing a smooth surface well suited for the subsequent growth of the desired Fe/Cr(001) layer system. Fe/Cr(001) superlattices with five to nine repeats of about 52 Å Fe and 9 to 17 Å Cr in each double layer were prepared. The evaporation rates were calibrated using the oscillations in the reflection high energy electron diffraction (RHEED) intensity, which indicate the completion of each monolayer. The superlattices were grown either at room temperature (RT) or at an elevated temperature (ET) of 250 °C starting with Fe and finishing with a protective ZnS layer on top of the last Fe layer. Due to the use of an extra Fe layer on top of the last Cr layer, an even number of equally thick FM layers was obtained in all samples. The Fe thicknesses were chosen to be quite large to achieve a large superlattice period

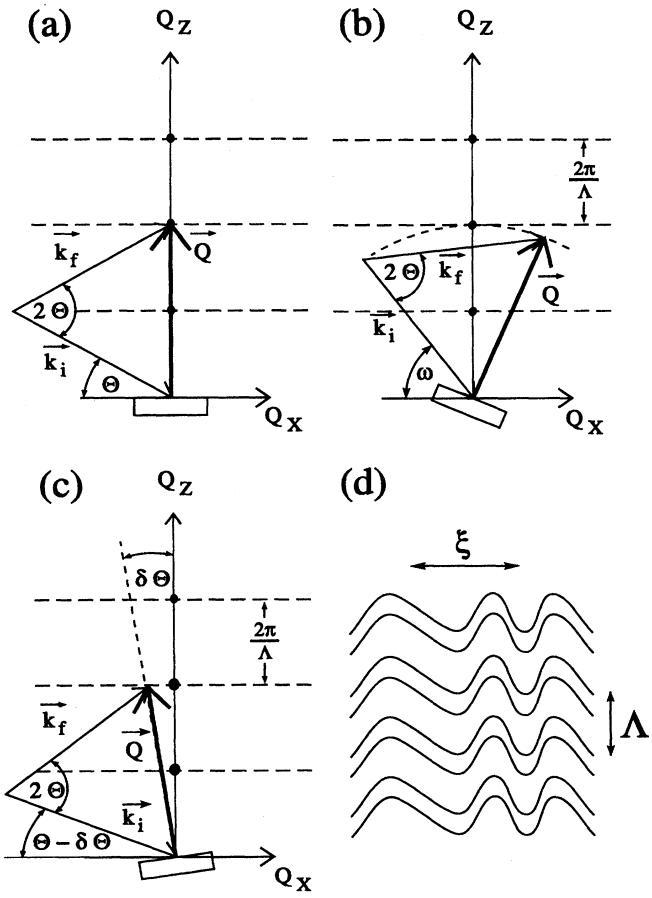

FIG. 1. "Ewald constructions" in reciprocal space for a (a) $\Theta/2\Theta$ scan measuring the specular intensity, (b) rocking curve measuring the off-specular and specular intensity, and (c) purely off-specular $(\Theta-\delta\Theta)/2\Theta$ scan. $\vec{k}_i$ and $\vec{k}_f$ are the wave vectors of the incident and final radiation, respectively. They define the scattering vector $\vec{Q}$. (d) Schematic cross-sectional view in real space of a multilayer with correlated roughness. The in-plane correlation length ξ can be approximated by the distance between the interface asperities. As shown in (a), (b), and (c), the double layer period Λ of the multilayer causes peaks along the Q_z axis (dots) separated by $2\pi/\Lambda$ and a corresponding intensity distribution of the diffuse intensity (dashed lines).

Λ leading to a small $2\pi/\Lambda$. This shifts the first superlattice peak to a small scattering vector $\vec{Q}$ with higher peak intensity in the x-ray and neutron reflectivities allowing for the use of small samples with a surface area of only 10×10 mm^2.

B. X-ray analysis

The structural characterization was carried out using a thin film diffractometer at a high intensity 18 kW rotating anode x-ray source using Cu K_α and Mo K_α radiation. To be able to distinguish between specular (coherent) and off-specular (diffuse) scattering, scans of the three types depicted in Fig. 1 were performed in the small angle regime. The specular intensity was collected using standard $\Theta/2\Theta$

scans along Q_z of type (a). This intensity results from coherent interferences and contains information, e.g., on internal periodic structures of the layered thin film system, leading to peaks which are marked by the dots on the Q_z axis. In addition, diffuse intensity can arise due to the existence of structural disorder in the sample. As opposed to the coherent intensity, it is not localized along the Q_z direction. Therefore, the scan types shown in Figs. 1(b) and 1(c) were used to map out the diffuse scattering. In scan type (b), mainly Q_x is varied, yielding information on the disorder in the lateral film plane, i.e., along the interfaces of a layered thin film system. In scan type (c), on the other hand, mainly Q_z is varied. This scan is especially useful when the sample's interfaces are correlated along the growth direction, as shown in Fig. 1(d). This correlation yields a fixed phase difference of the diffuse scattering from the single interfaces and thus leads to a coherent superposition. As indicated by the horizontal dashed lines in Fig. 1, this coherent superposition then generates similar maxima along Q_z as in the specular case. The scans of type (a) and (c) are also used to subtract the diffuse from the specular intensity, yielding the true specular intensity ready for data analysis. A more detailed description of these techniques is given in the paper by Savage *et al.*,[64] which also contains a comparatively simple formalism for the quantitative analysis of the diffuse spectra. The methods for the quantitative analysis of the specular data have been described elsewhere.[65,66]

To obtain information on the in- and out-of-plane crystalline structure, high angle measurements and grazing incidence diffraction (GID) (Ref. 67) measurements were carried out.

C. Polarized neutron reflectometry with polarization analysis

To determine the magnetic structure, PNR measurements were performed on the reflectometer BT-7 at the NIST research reactor. Instrumental and methodical details can be found elsewhere.[63,68–72] All four cross sections $(+,+)$, $(-,-)$, $(+,-)$, and $(-,+)$ were measured. Here $+(-)$ designates the up (down) polarization of the incident and reflected neutrons, defined relative to an applied field at the sample position. The first two non-spin-flip (NSF) reflectivities contain information both on the chemical structure via nuclear scattering and on the projection of the magnetic in-plane moment *parallel* to the polarization vector $\vec{P}$ of the incident neutrons, leading to a magnetic splitting of the otherwise degenerate $(+,+)$ and $(-,-)$ reflectivities. The last two spin-flip (SF) reflectivities, on the other hand, originate from any magnetization components *perpendicular* to $\vec{P}$. Thus, from a measurement and quantitative analysis of the NSF and SF reflectivities, magnitude *and* orientation of the in-plane magnetic moments, i.e., a completely vectorized magnetization profile can be mapped out. It is useful to define the axes parallel and perpendicular to $\vec{P}$ as the NSF and SF axes, respectively. The neutron data were corrected for diffuse background in analogy to the procedure for x rays described above. In addition, the data have been corrected for the efficiency of the various polarizing elements. A detailed account of these procedures can be found elsewhere.[73–75]

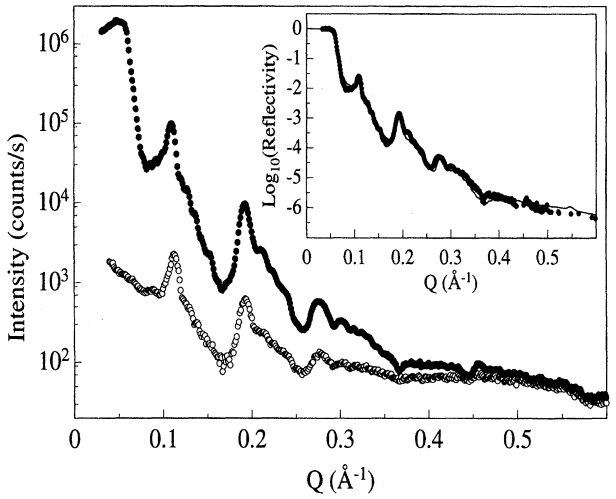

FIG. 2. Specular (dots) and off-specular (circles) x-ray data of the superlattice $[Fe_{52}/Cr_{17}]_9^{ET}$ taken with Mo $K\alpha$ radiation. In the inset the true specular reflectivity is shown together with a fit (solid line). For details see text.

D. Magneto-optic Kerr effect

As opposed to the *microscopic* spin structure determined by PNR, the MOKE is well suited for analysis of the *macroscopic* magnetic properties of thin film systems.[76] Nonetheless, MOKE only is sensitive to the resulting magnetization. Thus it cannot provide direct proof of microscopic spin structures and coherence lengths. The MOKE hysteresis curves were measured using a lock-in modulation technique providing a resolution of $\leq 5\times 10^{-4}°$.[77] The longitudinal geometry was employed with the external field parallel to the film planes. In this geometry, the method is sensitive to the resulting magnetization along the applied field direction.

III. STRUCTURAL CHARACTERIZATION

A. Small angle reflectivity

In Fig. 2 specular $\Theta/2\Theta$ (dots) and off-specular $\Theta-0.15°/2\Theta$ (circles) Q scans of the superlattice $[Fe_{52}/Cr_{17}]_9^{ET}$ are shown. Here the superscript ET stands for the elevated growth temperature of 250 °C. The numbers in the brackets give the respective layer thicknesses in Å, whereas the external subscript denotes the number of double layers. The data were taken with Mo $K\alpha$ radiation ($\lambda=0.7107$ Å) scanning along the directions shown schematically in Figs. 1(a) and 1(c). Specular and off-specular data are scaled to the same intensity, thus allowing for a direct comparison. At this wavelength, superlattice peaks up to the fifth order are clearly visible in the specular data. The fact that with increasing $|\vec{Q}|$ the specular and off-specular intensities coincide more and more shows how important a proper subtraction of the diffuse intensity is in this case. In the inset of Fig. 2, the true specular intensity, which remains after subtraction of the diffuse intensity, is plotted together with a theoretical fit to the data yielding an interface roughness $\sigma=3.5$ Å ≈ 2.5 monolayers (ML). Here σ is defined as the rms deviation $\sqrt{\langle z^2\rangle}$ from the ideal interface. From the

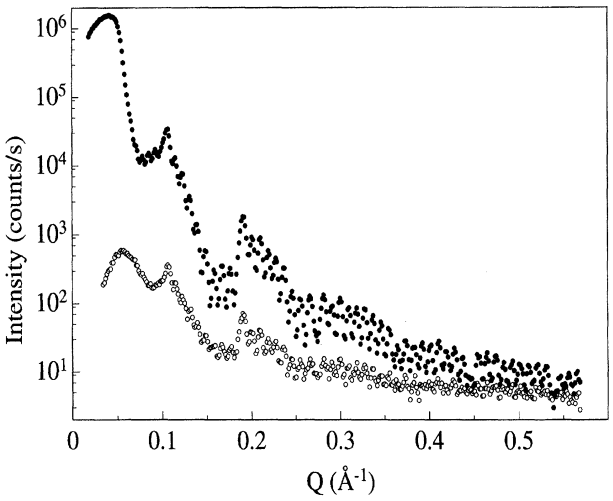

FIG. 3. Specular (dots) and off-specular (circles) x-ray data of the superlattice $[Fe_{52}/Cr_{17}]_9^{ET}$ taken with Cu $K\alpha$ radiation.

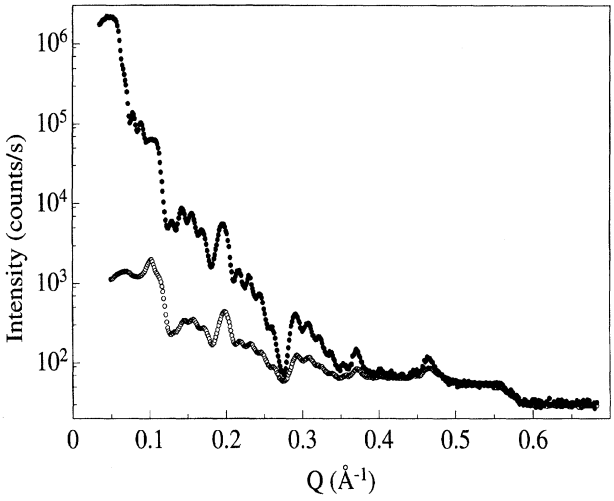

FIG. 4. Specular (dots) and off-specular (circles) x-ray data of the superlattice $[Fe_{52}/Cr_{17}]_5^{RT}$ taken with Mo $K\alpha$ radiation.

width and position of the superlattice peaks, we can exclude the possibility of any significant drift of the layer thicknesses during growth. The fit to the data became noticeably worse, as soon as a deviation from the Cr interlayer thickness by as little as one ML in either direction is assumed.

The off-specular (diffuse) intensity in the main part of Fig. 2 closely resembles the features of the specular data, thus indicating a significant correlation between the structures of the individual interfaces due to coherent superposition of their diffusely scattered intensities. In Fig. 3 equivalent specular and off-specular scans of the same sample measured with Cu $K\alpha$ radiation ($\lambda = 1.542$ Å) are shown. Due to different scattering contrasts and a better Q resolution at this wavelength, much stronger finite thickness oscillations are visible in the specular and off-specular scans. The most important feature here is that the off-specular data not only replicate the superlattice peaks of the specular data but also the finite thickness oscillations. Since the latter are caused by the coherent interference of well correlated top and bottom layers, their presence clearly indicates that the degree of correlation between the successive internal interface structures must also be very high. This qualitative argument is confirmed by a recent calculation by Payne and Clemens[78] who have studied the influence of the degree of correlation of the interfaces in $[Mo/Ni]_{20}$ multilayers on the diffuse scattering. Assuming an interface roughness of $\sigma = 2$ Å, they find that only a near perfect correlation between the individual interfaces results in diffuse finite thickness oscillations.

Comparison of Figs. 2 and 3 shows that more superlattice peaks are detectable when Mo $K\alpha$ radiation is used. Thus, with this radiation the interface roughness can be determined with higher accuracy for the present samples. The use of a Cu $K\alpha$ source is preferable when finite thickness oscillations must be resolved.

In Fig. 4, the specular and off-specular reflectivities of the superlattice $[Fe_{52}/Cr_{17}]_5^{RT}$ are shown, as measured with Mo $K\alpha$ radiation. Since the sample has the same layer thicknesses as the sample discussed above the data are quite similar to that of Fig. 2. The more pronounced finite thickness oscillations of period ΔQ are more clearly visible within the given Q resolution due to the smaller overall thickness D of the sample ($\Delta Q = 2\pi/D$). The data also show superlattice peaks up to fifth order, despite the significantly smaller number of bilayers $N_\Lambda = 5$ in this sample as compared to the previous sample with $N_\Lambda = 9$ (Fig. 2). This result indicates that the rms roughness is smaller for the present sample and suggests smaller rms interface roughnesses for RT-grown samples as compared to samples grown at 250 °C. This trend was observed in general for all samples investigated.

An important structural parameter accessible via measurements of the diffuse scattering is the *in-plane* correlation length ξ of the interfaces depicted in Fig. 1(d). As shown, e.g., by Savage *et al.*,[64] rocking curves are a simple way of determining ξ. These were introduced in Fig. 1(b). Typical rocking curves, as they were found for all samples, are shown in Fig. 5 for a sample of composition $[Fe_{52}/Cr_9]_5^{RT}$. The data were taken with Cu $K\alpha$ radiation at various fixed 2Θ values which correspond to the $|\vec{Q}|$ of the first-order superlattice peak (a), a finite thickness oscillation maximum in the region between the first- and second-order superlattice peaks (b), and the second-order superlattice peak (c) on the specular ridge (i.e., along Q_z), respectively. To accommodate all scans in one figure the ω values have been shifted such that the specular beam position always corresponds to $\omega = 0$. Thus the sharp component around $\omega = 0$ is the specular (coherent) intensity whereas the broader cusplike feature originates from diffuse scattering. At the smallest $|\vec{Q}|$ value Yoneda wings are clearly visible. They are a result of the enhanced transmission at those angular positions where the incident (exit) beam impinges (leaves) at the critical angle of total external reflection with the sample surface. At larger $|\vec{Q}|$ values the Yoneda wings are shifted away from the specular beam position into regions of smaller intensity of the diffuse cusp. In the present case, for $|\vec{Q}|$ corresponding to the second-order superlattice peak [Fig. 5(c)], the Yoneda wings are not visible anymore. This can be taken as an indicator that here optical effects are less important and that a purely kinematical approach is feasible. Such a kinematical

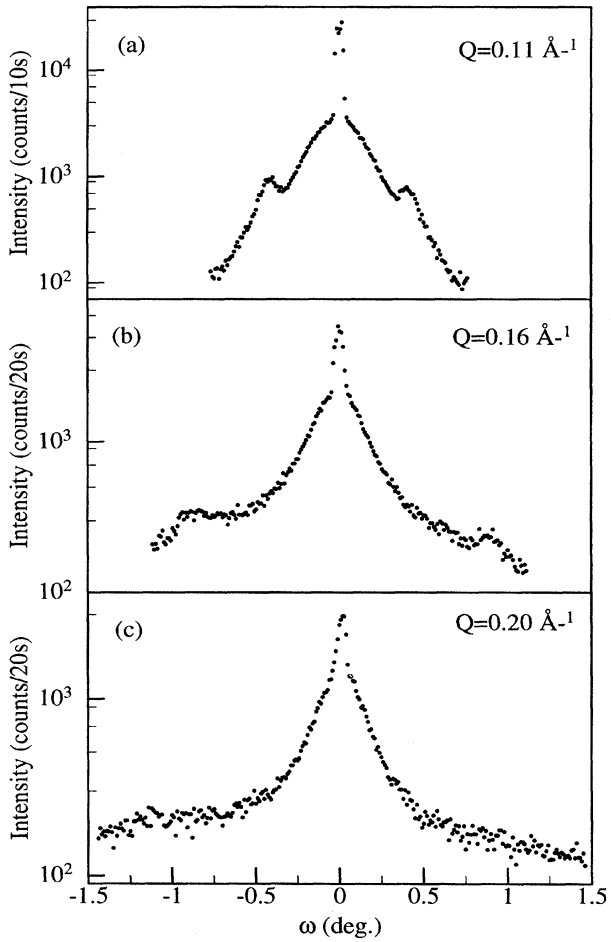

FIG. 5. Small angle rocking curves of a sample grown at RT at various Q as indicated in the figure and detailed in the text.

approach starts to become useful for scattering angles only a few times larger than the critical angle, since here the internal reflectivities are much smaller than one, and the optical effects of refraction, reflection, and multiple internal scattering become negligible. Therefore, the simple kinematical approach of Savage *et al.*[64] has been used to extract information on the in-plane correlation length ξ from rocking curves measured at large $|\vec{Q}|$ values, i.e., far above the critical angle. However, a simple conclusion about ξ can already be drawn at this stage. Corrected for the effect of the Yoneda wing, the width of all curves is about equal. This indicates that in all cases the diffuse scattering is determined by the same in-plane correlation length ξ.

Since diffuse scattering in multilayer systems can result from *vertically* correlated or uncorrelated roughness of the interfaces, a way to separate these must be found. Such a procedure follows from Fig. 1. The diffuse scattering from the correlated interface structures is strongly peaked along Q_z due to its coherent interference along $\hat{z}$. On the other hand, the diffuse scattering from any uncorrelated contribution to the roughness will be uniformly spread out along Q_z. Thus between the maxima of the off-specular intensity at $Q_z^n = n \times 2\pi/\Lambda$, $n = 1,2,\ldots$ *only* diffuse scattering from vertically uncorrelated interfaces can be present. As discussed in Ref. 64, this diffuse intensity should be smaller by a factor N_L, if the correlated and uncorrelated roughnesses are of equal magnitude. Here N_L is the number of layer pairs in the multilayer. In Fig. 6 the diffuse scattering from a multilayer with both a correlated and uncorrelated roughness component is depicted. Here, the in-plane correlation lengths ξ_c and ξ_u of the correlated and uncorrelated components were assumed to be different, as will be the most general case. Thus the rocking curves through $Q_z^n = n \times 2\pi/\Lambda$, $n = 1,2,\ldots$ and in between should be of significantly different intensity and width, the latter yielding ξ_c and ξ_u.

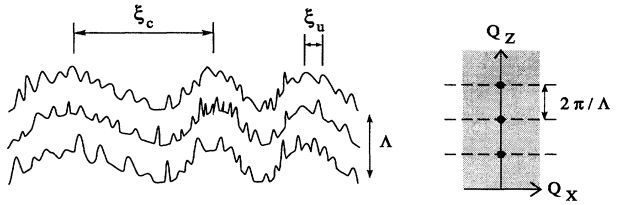

FIG. 6. Schematic cross-sectional view in real space (left) and the intensity distribution in Q space (right) for a multilayer with vertically correlated and uncorrelated roughness components which are characterized by the in-plane correlation lengths ξ_c and ξ_u, respectively. The correlated roughness leads to maxima in the off-specular (diffuse) intensity along Q_z (dashed lines) whereas the uncorrelated roughness causes diffuse intensity without such structure. Thus ξ_c can be determined using Q_x scans along the maxima in Q_z (dashed lines). ξ_u is obtained from Q_x scans between these maxima. For the angular range of interest the Q_x scans can be approximated very well by the rocking curves depicted in Fig. 1(b).

As shown in Figs. 3 and 4 above, the diffuse scattering of our Fe/Cr superlattices also exhibits strong finite thickness oscillations with period $\Delta Q = 2\pi/D$ in addition to the superlattice maxima at $Q^{\mathrm{SL}} = n * 2\pi/\Lambda$. Here D is the total thickness of the superlattice. This prominent feature was found to be due to the very high degree of correlation between the interfaces. Therefore, the diffuse scattering from any uncorrelated roughness component can only be measured between the finite thickness oscillations for the present samples. Thus, by performing rocking curves through maxima and minima of the finite thickness oscillations, ξ_c and ξ_u can be separated. It should be pointed out that from the equal widths of all rocking curves of Fig. 5 the same ξ_c follows for measurements through superlattice peaks and finite thickness oscillations. This result is a direct consequence of the high degree of correlation of all layers in the samples.

In Fig. 7, rocking curves measured with Cu $K\alpha$ radiation through a maximum and an adjacent minimum of a finite thickness oscillation are shown for two samples grown at 250 °C (ET) (a) and RT (b), respectively, together with fits employing the theory of Savage *et al.*[64] In the ET sample data, diffuse cusps of about equal form are visible in both rocking curves, indicating that ξ_c and ξ_u are of equal magnitude. The fits to the data, which should only be considered as rough order-of-magnitude estimates, yield about 2000 Å for both correlation lengths. The rocking curve of the RT-grown sample through the oscillation maximum yields a cusp of similar width leading to a ξ_c of about equal magnitude as for the ET sample. The rocking curve through the oscillation minimum in Fig. 7(b), on the other hand, does not

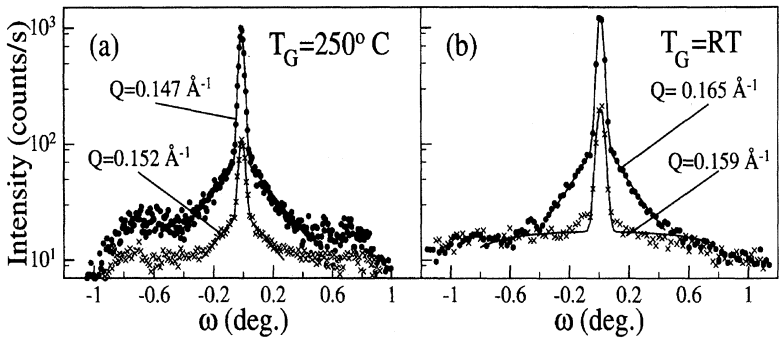

FIG. 7. Small angle rocking curves of two samples grown at 250° (a) and at RT (b) measured through two adjacent maxima (dots) and minima (crosses) of the finite thickness oscillations according to Fig. 6 with fits, as detailed in the text.

contain such a *symmetric* cusp around $\omega=0$. As opposed to Fig. 7(a), the diffuse scattering is only very slightly peaked around the specular beam position, which is consistent with a much smaller in-plane correlation length. The solid line was calculated for $\xi_u=50$ Å. However, this is only a rough estimate since for small ξ, i.e., for broad diffuse cusps, the fit is not very sensitive. In any case, comparison of the two rocking curves through the oscillation minima shown in Figs. 7(a) and 7(b) provides strong evidence for a difference by an order of magnitude or more between the ξ_u for both growth temperatures.

A schematic visualization in real space of the resulting structure for the sample grown at RT is provided by the left-hand side of Fig. 6. From the figure it follows that any uncorrelated roughness translates into a lateral layer thickness variation. Correlated roughness, on the other hand, does not affect the layer thicknesses. Thus from $\xi_u^{RT} \ll \xi_u^{ET}$ it follows that a significant growth temperature-induced difference exists in the length scale l on which the lateral layer thicknesses are constant.

Since l is an important parameter in the fluctuation and the proximity magnetism models introduced above, the next task is to estimate it. From the modeling of the specular reflectivity of the sample $[Fe_{52}/Cr_{17}]_9^{ET}$ $\sigma=2.5$ ML was found. Estimating the uncorrelated roughness component σ_u to be 1 ML and keeping in mind that for a given σ the deviation from the ideal interface can be more than 2σ, we obtain an *uncorrelated* interface fluctuation of more than ± 2 ML in the sample. Figure 8 schematically depicts the effect of such an uncorrelated fluctuation of ± 2 ML of two interfaces on the thickness of the interlayer between them. From the figure it follows that l would be about $\xi_u/16$, i.e., of order 100 Å. Any larger interface fluctuation will induce an average l below 100 Å. Consequently we arrive at $l \leqslant 100$ Å for the sample $[Fe_{52}/Cr_{17}]_9^{ET}$.

The correlated interface roughness is most probably induced by the Ag buffer acting as a rough template on all successive layers. The uncorrelated roughness then originates from the growth of the individual Fe and Cr layers. Consequently one would expect a decrease of the correlation of the top and bottom layers of the Fe/Cr system with an increasing number of layers. Experimental evidence for such a behavior is provided by the fact that the diffuse scattering is reduced in samples with fewer layers for the same growth temperature. More detailed modeling of the diffuse scattering from correlated and partially correlated multilayers using the distorted wave Born approximation (DWBA) would be required to study such growth models and to quantitatively confirm our interpretation of the data. Such modeling is very challenging and has been achieved only for less complex systems than the present one so far.[79] It remains a project for the future. However, the data of Fig. 7 by itself provide strong evidence that a growth temperature-induced difference in the length scale of the layer thickness fluctuations exists in the samples investigated.

Our results are consistent with very recent scanning tunnel microscope (STM) studies by Bürgler *et al.*[80] who have studied the growth of Fe and Cr as a function of growth temperature on the same GaAs/Ag substrate buffer system as used in the present work.

Furthermore, there is qualitative agreement with recent STM studies of the temperature dependence of the growth of Fe and Cr on Fe whiskers.[31,81] Whereas at elevated temperatures a growth mode close to layer by layer growth is achieved, leading to atomically flat layers over hundreds of Å, they obtained a significantly smaller length scale l for growth near RT. Consistently using RHEED Heinrich *et al.*[8] found a mean separation between atomic islands of monoatomic height of 700–800 Å for growth near 300 °C on Fe whiskers. Thus the trend in the effect of the growth temperature is the same, whereas the length scale of constant thickness l is found to be larger than reported here. This is most likely due to the use of smoother substrates than in our case, offering fewer steps for subsequent growth.

Before the effects of the interface structure on the magnetic behavior are discussed, the results of the high angle scattering experiments will be reported in the following section.

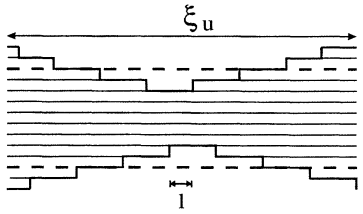

FIG. 8. Schematic illustration of the effect of a vertically *uncorrelated* interface fluctuation of ± 2 ML for a given ξ_u on the interlayer. The dashed lines indicate the two ideal interfaces. Assuming equal lengths of all terraces, the terrace length of every interface will be about $\xi_u/8$ as a result of the fluctuation. Due to the complete absence of any vertical correlation, the second interface will fluctuate independently, leading to a length scale of constant interlayer thickness l which on average is about half of the terrace length, i.e., $\xi/16$.

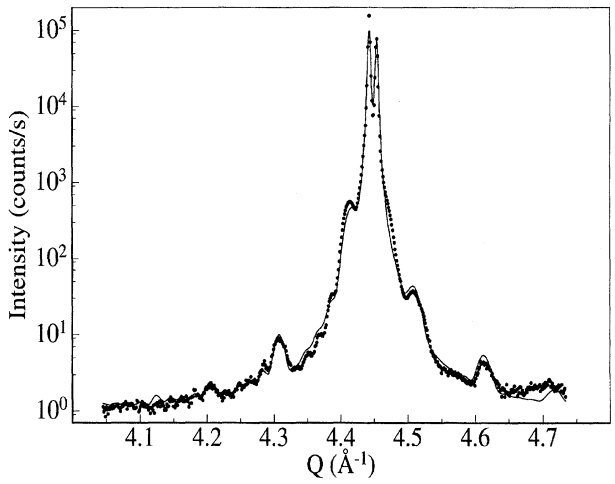

FIG. 9. High angle x-ray data of the superlattice $[Fe_{52}/Cr_9]_5^{RT}$ and a model calculation (solid line). For details see text.

B. Crystalline structure

Whereas, in the small angle regime, information on the layered system as a whole and the interfaces between them is accessible, additional information on the crystalline structure can only be obtained at large scattering angles. In Fig. 9 a longitudinal scan in the [001] direction of a sample with composition $[Fe_{52}/Cr_9]_5^{RT}$ taken with Cu $K\alpha$ radiation is shown. The most intense and split peak around $Q \approx 4.44$ Å^{-1} is due to the GaAs buffer. The splitting is caused by the characteristic Cu $K\alpha_1$ and Cu $K\alpha_2$ lines which differ in wavelength by 0.25%. Just left of the GaAs signal the bcc Fe/Cr(002) fundamental peak is observed. The periodic modulation of the superlattice is demonstrated by the first- and second-order superlattice peaks which are visible on both sides of the main peak. The additional finite thickness oscillations between these peaks indicate that the coherence length is close or equal to the overall thickness of the Fe/Cr layer system. The solid line in Fig. 9 is a fit[82] to the data, yielding $\sigma \approx 1.5$ ML.

For samples grown at 250 °C, similar Bragg scans were obtained. However, as indicated by the absence of higher-order superlattice peaks in most cases, the only significant growth temperature-induced difference between the samples is a larger crystal plane roughness at the interfaces. This is consistent with the results of the small angle reflectivity measurements.

For all samples, and independent of the growth temperature chosen, the out-of-plane lattice parameters (i.e., along the growth direction of the film) were found to be equal within the accuracy of the measurement. The coherence length of the average lattice was always close or equal to the overall film thickness and the mosaic spread, defined as the full width at half of the maximum intensity (FWHM) of a rocking curve through the fundamental Fe/Cr(002) peak, was about 0.2°–0.3°. As it turns out, the mosaic spread of the Ag buffer, as determined from the out-of-plane Ag(002) peak, is of the same magnitude. Therefore it seems that, independent of growth temperature, the mosaic spread of the Fe/Cr layer system is induced by the Ag buffer.

In order to characterize the crystalline quality in the film plane, grazing incidence diffraction (GID) (Ref. 67) experiments were performed. This special scattering geometry combines elements of small angle reflectivity and high angle Bragg scattering. By tuning the incident angle to the critical angle of total external reflection Q_C, i.e., to the maximum of the transmission function, the maximum intensity of an evanescent wave in the Fe/Cr is achieved. The in-plane Bragg-scattered intensity yields information on the *in-plane crystalline structure*, i.e., on the lattice constant perpendicular to Q_z. The in-plane mosaic spread was found to be 0.2° independent of the sample's growth temperature. The in-plane lattice constants were equal for all investigated samples. The in-plane coherence length was found to be about 330 Å for all samples, again independent of the growth temperature.

C. Conclusions

In summary, it can be stated that no growth temperature dependence of the crystalline structure of the Fe/Cr superlattices was detected within the accuracy and resolution of the diffractometer. Both high and small angle measurements indicate a smaller rms roughness at the interfaces for most of the RT-grown samples. From the specular and off-specular small angle reflectivity data it was found that there is a high degree of vertical correlation of the interfaces throughout the layer stack in all samples. Furthermore, ξ_c was determined to be about equal for all samples. This suggests that the strongly correlated interface structure could be induced in the same way for all samples by steps on the surface of the Ag buffer. These steps would then propagate through the Fe/Cr layer stack, governing the strong correlation even between the top and bottom layers. Similarly the Ag buffer also seems to be responsible for the crystalline mosaic spread of about 0.2°. In this picture the uncorrelated component of the roughness is due to the growth mode of the Fe and Cr layers which, in turn, depends on the growth temperature. This explains the observed differences in ξ_u at high and low growth temperatures. The smaller ξ_u for RT samples translates into interlayer thickness fluctuations on a much shorter length scale as compared to the ET samples. This difference has a pronounced effect on the magnetic exchange coupling, as will be shown in the remainder of this paper.

IV. MICROSCOPIC AND MACROSCOPIC MAGNETIC PROPERTIES

A. Noncollinear coupling

1. Results near remanence

To confirm the existence of a noncollinear magnetization profile in the samples grown at 250 °C PNR scans were performed on such superlattices.

In Fig. 10 PNR data[60] of the superlattice $[Fe_{52}/Cr_{17}]_9^{ET}$ measured in a field of $B_{GF} = 17$ G are shown together with model calculations (solid and dotted lines). The $(+,+)$ and $(-,-)$ cross sections are indicated by dots and circles, respectively. The SF cross sections were measured to be equal and were added to improve counting statistics. They are plotted as inverted triangles referring to the scale on the right axis. As indicated in the inset, the external field was applied along one of the sample's easy axes (dashed lines). Prior to

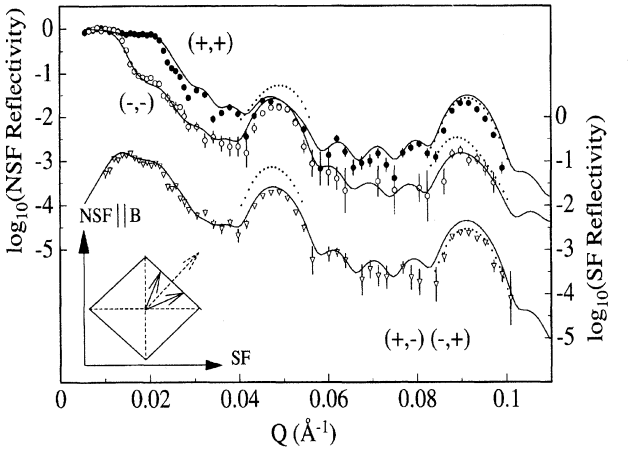

FIG. 10. PNR NSF (top) and SF (bottom) data of the superlattice $[Fe_{52}/Cr_{17}]_9^{ET}$ together with theoretical calculations assuming coupling angles of 90° (dotted lines) and 50° (solid lines). The latter case is depicted in the inset. For details see text.

the measurement the field was increased to 7300 G and subsequently slowly lowered to 17 G using an electromagnet. This procedure provides a well known "magnetic history." PNR measurements were not performed in zero field at the sample position, since in this case no neutron quantization axis would exist, leading to a depolarization of the neutrons. Also shown in the inset are the NSF and SF axes, which define the parallel and perpendicular components of the in-plane magnetization relative to the neutron polarization direction $\vec{P}$, respectively.

The data exhibit a large splitting in the NSF cross sections. First-order superlattice peaks at $Q_1 = 2\pi/\Lambda \approx 0.9$ Å^{-1} and half-order peaks at about $Q_{1/2} = 2\pi/2\Lambda$ occur in all cross sections. The fact that all peaks exhibit the same width shows that the nuclear and magnetic coherence lengths are equal, indicating a well defined and coherent magnetic order throughout the whole film thickness. From the discussion of Sec. II C, the magnetization profile of the sample can be qualitatively inferred. The splitting of the NSF data, together with the existence of the SF peak at Q_1, indicates a significant resulting magnetization in *each* Fe layer with components parallel to the NSF *and* the SF axes. The strong half-order peaks in all cross sections, on the other hand, are direct proof of a doubling of the magnetic period as compared to the nuclear superlattice period for magnetization components along the NSF and SF axes. These two observations require a magnetization profile which, on one hand, oscillates in the plane between two angles to provide the doubling of the magnetic superlattice period, and on the other hand forms a resulting moment along the NSF and the SF axes. Consequently, the angle between neighboring Fe layers cannot be 180° (collinear, AF coupling) since, due to the even number of Fe layers in the system, in this case no resulting moment would exist.[61] A noncollinear magnetization profile is required instead, e.g., as indicated in the inset of Fig. 10 by the solid arrows.

Due to the two easy axes 90° apart and the small applied field, it is tempting to assume a coupling angle of 90°. This would agree with the initial domain observations by Kerr microscopy and the MOKE measurements on wedged trilayers by Rührig *et al.*[23] It must be pointed out, however, that those data were obtained from samples grown at RT whereas the present sample was grown at 250 °C. As already indicated, a change in growth temperature drastically changes the sample's properties. As shown in Fig. 10 by the dotted lines the simplest model of a coupling angle of 90° leads to much larger expected half-order intensities in all cross sections than observed experimentally. In this calculation, the existence of only one domain in the sample with the layer magnetizations oriented along the two easy axes has been assumed. However, near remanence the existence of domains is expected and must be taken into account in the modeling. Further below in Sec. IV A 2 we will show first that domains only complicate the modeling very close to remanence, and second that contrary to an earlier suggestion of ours,[60] the presence of domains does not significantly affect the scattering. Therefore, the discrepancy between the 90° model and the data of Fig. 10 indicates that the coupling angle is not 90°.

In principle there are two ways to superimpose the scattering from different regions (e.g., magnetic domains) of a sample. In the case of *incoherent* superposition the average of the reflected *intensities* $|\mathscr{R}^j|^2$

$$|\mathscr{R}|^2 = \sum_j c_j |\mathscr{R}^j|^2 \tag{3}$$

is taken, where the c_j denote the relative contribution from domain type j with $\Sigma_j c_j = 1$. For a *coherent* superposition the *amplitudes* $\mathscr{R}^j$ are first added and then the sum is squared:

$$|\mathscr{R}|^2 = \left| \sum_j c_j \mathscr{R}^j \right|^2 . \tag{4}$$

We note an important difference between the two procedures. In the coherent case, the scattering from oppositely aligned moments of equal magnitude in one magnetic layer is canceled. Thus, in the scattering from such a magnetic layer, no magnetic moment would be observed. In the case of incoherent superposition, on the other hand, no such cancellation effect occurs.

The data can be fitted quite well assuming a single domain and allowing the orientation of the magnetic moments in successive Fe layers to deviate from 90°. With an accuracy of a few degrees, the coupling angle is found to be 50°. The layer magnetizations are oriented symmetrically with respect to the two easy axes as depicted in the inset of Fig. 10. It turns out, however, that the exact stacking sequence of the layers affects the modeling of the (+,+) data. The two possible stacking sequences for a given orientation of the magnetic moments are shown schematically in Fig. 11(a). In Fig. 11(b) the eight different domain types are shown which could occur in the system near remanence for the given in-plane anisotropy. The arrows with full lines describe the moment orientation of the first, third, fifth, etc. Fe layer whereas the one with the dashed line corresponds to the moment orientation in the second, fourth, sixth, etc. Fe layer. The half-order peak positions and intensities of the calculated (+,+) reflectivity differ somewhat from the data, if

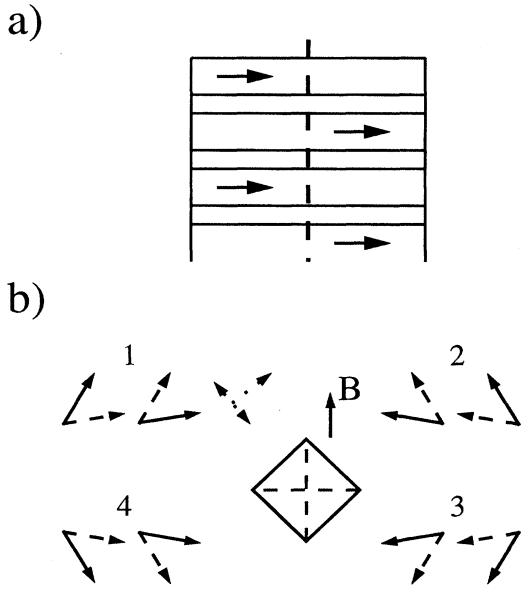

FIG. 11. (a) Schematic side view of a superlattice sample with two domain types, which only differ in stacking sequence. (b_1)–(b_4) Top view of the eight different domain types which are allowed for near remanence by the magnetic in-plane anisotropy. The two easy axes of the latter are indicated by the dashed lines in the square in analogy to Fig. 10. The direction of the external magnetic field is also shown. The eight possible domain types are divided into four groups by orientation of their resulting moment. Within each group the two domain types only differ by stacking sequence analogous to (a), as indicated by the two different types of arrows. The angle between the arrows was chosen to coincide with the measured value of 50° (see text). Equivalent domains would occur for a coupling angle $\varphi_c = 90°$, with the moments oriented along the easy axes. The additional dotted arrows in (b_1) show how the two possible moment orientations in each FM layer shown on the left-hand side can be decomposed into parallel and antiparallel components.

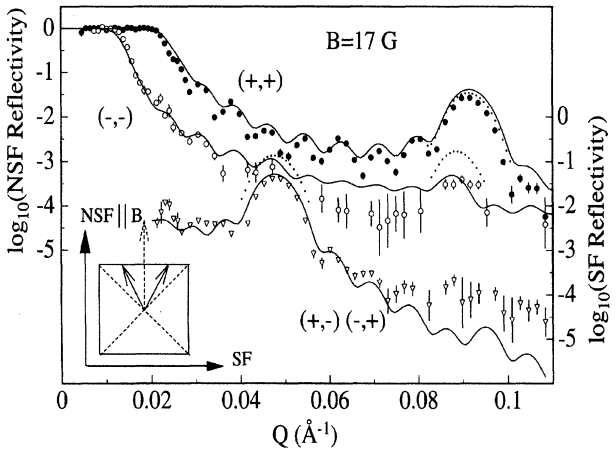

FIG. 12. PNR scan of the superlattice $[Fe_{52}/Cr_{17}]_9^{ET}$ oriented with the resulting magnetization parallel to the NSF axis, as indicated by the inset. The solid line is a calculation assuming a coupling angle of 50°, as shown in the inset. The dotted line shows a corresponding calculation with a coupling angle of 90°.

either of the two possible stacking sequences shown in Figs. 11(a) and 11(b_1) is assumed. If, on the other hand, an *incoherent* summation over the scattering from these two domain types according to Eq. (3) with $c_1 = c_2 = 0.5$ is performed, the solid line in Fig. 10 is obtained. This model fits the half-order intensity of all cross sections best.

Due to the sensitivity of PNR with polarization analysis to the orientation of the in-plane magnetic moments, a rotation of the sample around an axis perpendicular to the sample plane will have a significant effect on the reflectivity. In this way any model of the spin structure can be tested by rotating the sample. In the present case, a counterclockwise rotation of the sample by 45° should lead to a larger splitting of the NSF cross section since the resulting moment (dashed arrow in the inset of Fig. 10) would now be parallel to the NSF axis. Furthermore, half-order peaks should only occur in the SF cross sections since the projections of all layer magnetizations onto the NSF axis are now equal. As shown in Fig. 12 these are exactly the features observed experimentally. The sample is oriented now as depicted in the inset and the same symbols as in Fig. 10 are used. The guide field $\vec{B}_{GF}$ was lowered to about 5 G during and after the rotation to minimize any influence on the magnetization profile of the sample. If the coupling angle were 90° and the moments were oriented along the easy axes (dashed lines in the insets of Figs. 10 and 12) the same qualitative arguments for the effect of the sample reorientation would hold as for the 50° magnetization profile. The fit, however, clearly favors the 50° model over the 90° model as shown in Fig. 12. In contrast to the previous sample orientation we find here that the fit procedure is insensitive to the specific incoherent summation over the two assumed 50° domain types.

The result of a 50° coupling angle follows not only from the half-order intensities in all cross sections but also from the splitting of the NSF cross sections, e.g., at the first-order peak position. Since this splitting is determined by the projection of the resulting moment onto the NSF axis (dashed arrow in the inset of Fig. 12) and since for the turned sample orientation this projection is largest, the data of Fig. 12 are expected to be most sensitive to such differences induced by the coupling angle. Again, inspection of the data clearly shows that it is the 50° coupling angle which reproduces the large NSF splitting observed at the first-order peak position. The same trend is visible in Fig. 10, but the effect is smaller due to the smaller projection of the resulting moment onto the NSF axis.

Furthermore, it should be pointed out that the model fitting is unique in the following sense: First, the results of the quantitative analysis of the x-ray data (Fig. 2) have been used as input for the modeling of the chemical structure. Second, from PNR in the saturated state the magnitude of the Fe moments was found to be the bulk one. Consequently the only fitting parameter left is φ_c, the coupling angle between the layer magnetizations. If the φ_i, $i = 1,2$ describe the orientation of the first, third, fifth, etc. layer ($i = 1$) and of the second, fourth, sixth, etc. ($i = 2$) layer magnetization relative to the applied field direction, then φ_c is given by

$$\varphi_c = |\varphi_1 - \varphi_2|. \quad (5)$$

This definition is justified because the width of all observed peaks reflects a coherent magnetic stacking throughout the entire sample. Furthermore, in the turned sample position shown in Fig. 12 the layer moments are oriented symmetrically with respect to the NSF axis. Therefore, in addition the relation $\varphi_1 = -\varphi_2$ holds. Then the only fitting parameter left is φ_c providing the result of $\varphi_c = 50°$ with an even higher degree of confidence.

Finally, this result correlates well with PNR data as a function of external field along the easy and hard axes as will be shown in detail below in Sec. IV A 3.

2. Influence of domains on the scattering

So far it has been shown that the data near remanence can be explained very well with $\varphi_c = 50°$ as long as it is assumed that purely *incoherent* averaging applies over any domains in the sample. Furthermore, only two domain types, which only differ in stacking sequence, had to be assumed to perfect the modeling of the data. In the following we will show that both assumptions are correct, i.e., that other domain types or a coherent contribution to the domain averaging would have significantly altered the measured PNR spectra.

a. Coherent averaging. As discussed in detail in Ref. 60 the data of Fig. 10 are only consistent with a coupling angle of 90° if the two specific types of magnetic domains shown in Figs. 11(a) and 11(b_1), modified for a coupling angle of 90° instead of 50°, are assumed. Furthermore, a mixed incoherent-coherent averaging process over these domains has to be postulated to be able to reproduce the observed half-order intensities in all cross sections. The coherent contribution to the averaging is required since it can be used to reduce the calculated half-order intensity to a value consistent with the data. In the extreme case of a purely coherent averaging, no half-order intensity would exist at all in a calculated spectrum, although the assumed magnetic structure still has twice the period of the nuclear structure. This is a direct consequence of the peculiar cancellation effect on oppositely aligned magnetic moments in one layer, mentioned above in the discussion of Eq. (4). If we assume the domain structure of Fig. 11(b_1) with an equal number of both domain types in each layer, we can think of the magnetic structure of one layer as being decomposed into the three components shown in Fig. 11(b_1) by the dotted arrows. As is confirmed by the model calculations, purely coherent superposition will cancel out the oppositely aligned components. This is why the sensitivity to the doubling of the magnetic over the nuclear unit cell is removed for purely coherent superposition in this case. The question which has to be answered now is if any coherent superposition is acceptable in the modeling or not. If not, there is no way the measured spectra can be consistent with a 90° coupling angle.

First, we briefly want to consider the role of the coherence length of the incident neutrons. Following Rauch[83] the component of the neutron coherence length parallel to the sample surface, $l^{\parallel}$, is on the order of 2 cm for our reflectometer. This value is much larger than for x rays due to the dominant role of dispersion for neutrons. Since $l^{\parallel}$ is larger than the diameter of our samples one could conjecture that purely coherent averaging over all domains in the samples takes place. However, from the discussion above it follows that no half-order intensity would have been observed at all in this case. Consequently the length scale of coherent averaging rather seems to be determined by the sample itself and $l^{\parallel}$ only is an upper limit.

To determine the role of coherent superposition in detail, PNR spectra as a function of external magnetic field have been taken with very small field steps. Furthermore, Kerr microscopy has been performed as a function of external field on the same sample and in the same orientation to determine when domains nucleate upon field reduction. Only at the domain nucleation field can any coherent contribution to the averaging occur, since above this point the sample is in a single domain state. The PNR measurements reveal a *continuous* change of intensity at the half-order peak positions in all cross sections due to the continuous field dependent variation of the coupling angle. This fact clearly indicates the absence of any coherent averaging contribution. If there were a coherent contribution to the averaging a *discontinuous* jump of the half-order peak intensity should occur upon domain nucleation. The corresponding difference in half-order intensities in all cross sections can be obtained from Fig. 10 for the specific case of a coupling angle of 90°. Here the dotted line corresponds to the single domain case whereas the measured data would represent the intensities in the 90°-coupled two-domain-type state. Thus we conclude that we cannot use any coherent averaging contribution in our modeling. This invalidates our initial incoherent-coherent multidomain 90° model,[60] which we proposed when we had no further data than the one discussed at that time. We will demonstrate below that all data taken since then actually are inconsistent with our initial model.

Now that we have good evidence that no coherent contribution to the domain averaging exists we have to justify the domain types assumed in the modeling of the data of Figs. 10 and 12.

b. Domain types. From Fig. 11(b_1) we see that both domain types assumed in the modeling have the same resulting moment. Coherent and incoherent averaging over these resulting moments will make no difference since no cancellation effect occurs in this case. Therefore, the determination of the resulting moment from the PNR data is model independent and can be used for a direct comparison between the data and the various possible magnetic structures without any further assumptions. Since the resulting moment directly translates into a NSF splitting and a SF first-order peak intensity in the PNR data, these quantities are *independent of the averaging process.*

First, it must be noted that the magnitude of the resulting moment is a direct measure of the coupling angle. Thus it is ideally suited for the determination of the coupling angle, independent of the averaging process. As discussed above, comparison of the calculations for $\varphi_c = 50°$ and $\varphi_c = 90°$ shown in Figs. 10 and 12 clearly confirms $\varphi_c = 50°$, independent of the averaging process.

Second, if any other domain types would exist in the sample, they would have to differ in the orientation of the resulting magnetic moment from the ones shown in Fig. 11(b_1). However, due to the fourfold in-plane anisotropy, the easy axes of which are also shown in Fig. 11(b), only four possible orientations of the resulting moments would be energetically favorable near remanence. These are the ones shown in Fig. 11(b_1–b_4). The presence of orientations 3 and

4 would drastically affect the NSF splitting since the $(+,+)$ and $(-,-)$ cross sections are inverted for these domain types. Such a contribution is inconsistent with the modeling. Furthermore, before the PNR measurements the sample was saturated and then the field was reduced to a small value near remanence. This procedure makes orientations 3 and 4 highly unlikely anyway. Thus, independent of the averaging process, the modeling of the NSF splitting confirms the absence of these domain types. In the case of an exact alignment of one easy axis with the external field axis, moment orientations 1 and 2 should be equally probable. In a realistic situation, however, any small deviation from this perfect alignment will strongly favor one orientation over the other. We therefore expect only either type 1 or 2 to occur. The distinction between these two orientations can then be made by turning the sample counterclockwise, as described above. Only in the case of moment orientation 1 is the spectrum of Fig. 12 expected. For orientation 2 the half-order peak would be expected in the NSF cross section instead. Thus, of the four different possible orientations, we can safely exclude the presence of three. If not in the orientation of the resulting moment, the only other way the domains in our sample can differ is in stacking sequence. As detailed above, we find very good agreement with the data when assuming the equal presence of the two domain types of orientation 1 in the modeling of the PNR data.

As already mentioned, Kerr microscopy has been performed on the present sample. Since to our knowledge the contrasts for the various domain types discussed here are not yet understood for samples with more than three layers, it was not possible to do a quantitative analysis of the contrasts along the lines of the work by Rührig *et al.*[23] Currently such studies are under way in the group of Hubert on wedge shaped Fe/Cr(001) trilayer samples grown at 250 °C. However, it was possible to observe the *occurrence* of domains upon field variation. The topology of the domain walls, which contains information on the domain types in the sample,[23] was observable as well. The domain walls were irregularly shaped, indicating that the domains in the sample all have the same direction of net magnetization.[23] If neighboring domains had different orientations, domain walls with straight sections should have been observed. From this we conclude again that domains in our sample do not differ in their magnetization direction but only in their stacking sequence. Therefore, the Kerr microscopy appears to confirm the domain structure which we obtained from the modeling of the PNR data.

Finally, it should be pointed out that the data of Figs. 10 and 12 cannot be explained by a superposition of scattering from ferromagnetically and antiferromagnetically coupled regions of the sample. This follows from the observed data when the known in-plane anisotropy in the system is taken into account. For example, for the case of Fig. 10 any FM component should basically be oriented along the NSF axis, i.e., an easy axis, due to the initially applied field. The existence of the strong first-order SF peak clearly contradicts this picture. After the reorientation of the sample this FM component would still be oriented along the same easy axis. This should lead to a strong first-order SF peak in Fig. 12 which obviously is not observed. Therefore, only a noncollinear magnetization profile explains the data.

In conclusion, we have been able to exclude the presence of any other domain type than the ones assumed in the quantitative analysis of the PNR data of Figs. 10 and 12. Furthermore, we found that no coherent contribution to the domain averaging exists. Thus noncollinear coupling is observed near remanence with $\varphi_c = 50°$ instead of the 90° found so far. However, the magnetic domains, which complicate the analysis of the data somewhat, only exist close to remanence. At higher fields the sample has only one magnetic domain, making the data analysis much simpler.

3. Field-dependent measurements

If the external field at the sample position is varied, the whole range of magnetization profiles between saturation and the ground state in $B \approx 0$ can be mapped with PNR. Such measurements have been performed with an electromagnet in a range of $5 \leq B \leq 7300$ G along the hard and the easy axes. The sample orientations of Figs. 12 and 10, respectively, correspond to these two configurations. An important result is that the spectrum of Fig. 12 can alternatively be obtained by saturating the sample along a hard axis and subsequently reducing the field to the minimal guide field, i.e., with an equivalent magnetization process as applied in the case of Fig. 10. Therefore, the 50° magnetization profile found consistently for both sample orientations is the ground state of the system near remanence.

A few representative field dependent spectra are plotted in Fig. 13 together with model calculations. To account for the limited available beam time, the reflectivities were measured only in the total reflectivity, half-order peak, and first-order peak regions. Comparison of Figs. 10, 12, and 13 demonstrates that the intensities of the NSF $(-,-)$ and SF half-order peak intensities are good indicators of the magnetization profile and orientation. In Fig. 14(a) these peak intensities, as measured upon reducing the field from its maximum value, are plotted as a function of applied field. Whereas the NSF half-order intensity remains below background level [dashed line in Fig. 14(a)] down to about 310 G, the SF half-order peak evolves between 4 and 5 kG. For larger fields spectra like the one in Fig. 13(a) are observed. When the field is reduced further, the SF half-order intensity increases up to a maximum value. According to the discussion above, the existence of a half-order peak *only* in the SF channel implies a magnetization profile with the resulting moment parallel to the applied field, i.e., the NSF axis. The increasing intensity of the SF half-order peak then is a measure of the growing φ_c due to an increasing projection onto the SF axis. Below about 310 G, an additional NSF $(-,-)$ half-order peak evolves, indicating a turning process of the layer magnetizations in the sample which is reminiscent of the sample turning process discussed above. Close to remanence the data of Fig. 10 are recovered. As mentioned above, PNR was not measured in zero field due to the loss of a well defined neutron polarization axis.

From Figs. 10 and 13 it is evident that the half-order peak width does not change significantly during field variation in the low field region. This indicates that basically all layers rotate coherently, making the definition of a single angle φ_c between the layer magnetizations meaningful. However, some minor half-order peak broadening is visible at higher fields (above about 1 kG). Keeping in mind that the outer-

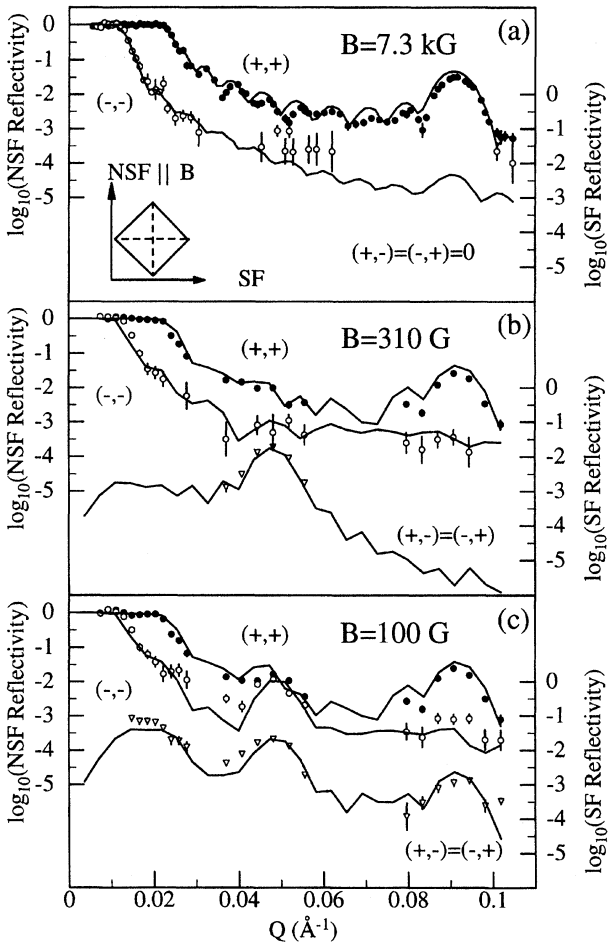

FIG. 13. PNR spectra of the superlattice $[Fe_{52}/Cr_{17}]_9^{ET}$ as a function of applied field along an easy axis, as indicated in the figure.

most layers are only coupled to one neighbor, whereas the inner ones have two neighbors, we expect that the outer moments have a somewhat different orientation in an applied field. The induced disorder leads to a peak broadening particularly of the half-order peaks. This effect is small, however, in the present case and is not important for the following considerations.

The quantitative analysis of the complete data sets in all cross sections over the whole Q range, and as a function of the applied field, yields the angles φ_1 and φ_2, as indicated schematically by the arrows in Fig. 14(a). Some representative fits are shown in Fig. 13. Above 4.9 kG the spectra appear saturated. However, quantitative analysis indicates that angles $\varphi_c \leq 5°$ cannot be distinguished, because the corresponding SF half-order peak intensity is below the given (very low) background level [dashed line in Fig. 14(a)]. In principle, any nonzero φ_c will also reduce the NSF splitting but this effect is too small to be analyzed with sufficient confidence. Upon lowering the field, the analysis shows that the angles gradually open up from $\varphi_c \leq 5°$ at 4.9 kG to $\varphi_c = 28°$ at 310 G [Fig. 13(b)]. Below 310 G an additional turning process is superimposed onto a further increase of φ_c. Near remanence the $\varphi_c = 50°$ ground state, depicted in Fig. 10, is reached with the layer magnetizations as close to the easy axes as allowed for by the 50° coupling angle. Since the in-plane anisotropy favors an alignment of the layer magnetizations parallel to the easy axes, it is plausible that the observed turning process is anisotropy induced. Furthermore, the observed magnitude of φ_c will be the result of a competition between the exchange coupling and the in-plane anisotropy. A more detailed discussion of the role of the in-plane anisotropy will be presented further below.

For comparison the MOKE hysteresis of the same sample, normalized to the Kerr rotation in saturation and measured in the same sample orientation, is plotted in Fig. 15(b). A gradual decrease of the observed Kerr rotation is observed indicating the increase in φ_c. The onset of the anisotropy induced turning process correlates with a dramatic change in the slope of the MOKE curve. The MOKE still shows a very small change above 4.9 kG where the quantitative analysis of the PNR data cannot distinguish clearly between $\varphi_c \leq 5°$ and saturation. Consequently, due to the absence of any comparable background, MOKE appears to be more sensitive to small deviations from the saturated state in the present case.

In Fig. 14(b) the results of the quantitative analysis of the PNR data are presented in a form which allows a comparison with the MOKE data. The large dots were obtained by calculating the sum of the components of all individual layer magnetizations along the applied field as obtained from the analysis of the PNR data using the relation

$$\frac{M(B)}{M_S} = \frac{1}{2}[\cos(\varphi_1(B)) + \cos(\varphi_2(B))], \tag{6}$$

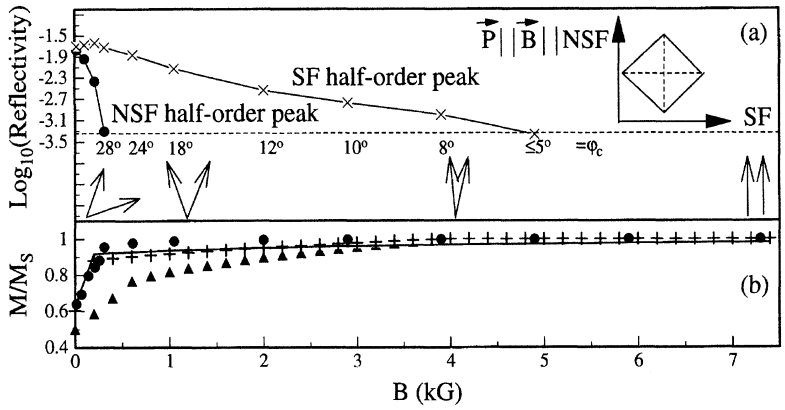

FIG. 14. (a) PNR NSF $(-,-)$ (dots) and SF (crosses) half order peak intensities for the superlattice $[Fe_{52}/Cr_{17}]_9^{ET}$ and (b) M/M_S (large dots) as obtained from the quantitative analysis of the PNR data with theoretical calculations according to the bilinear-biquadratic exchange energy (crosses, triangles) and using the exchange energy based on proximity magnetism (line). (a) and (b) are plotted against the external field which was oriented along an easy axis.

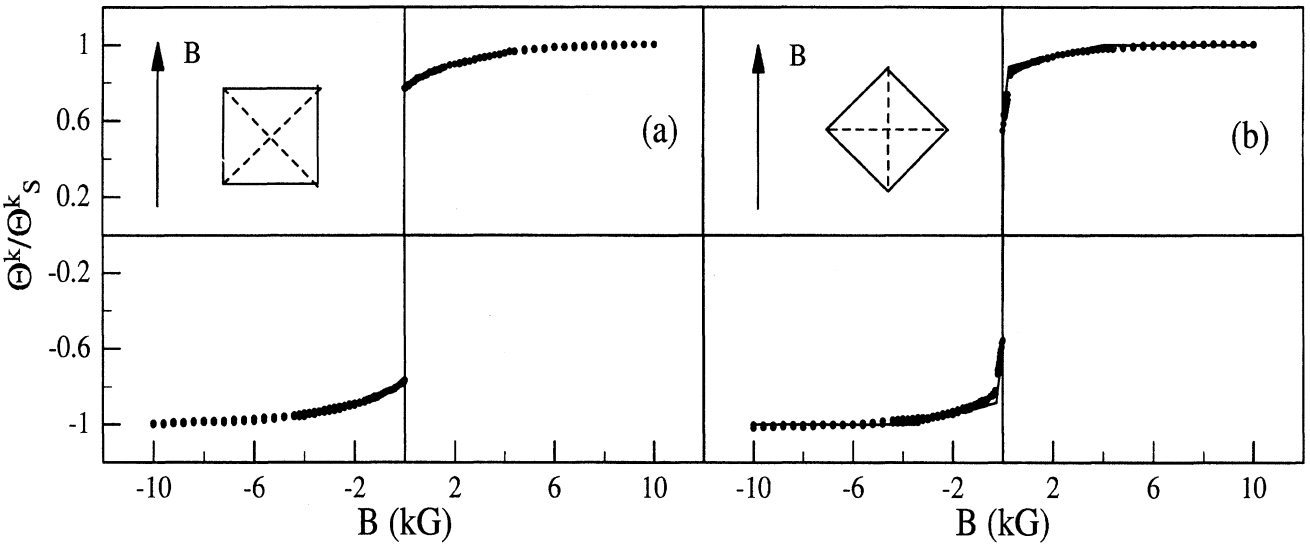

FIG. 15. MOKE hysteresis curves, normalized to the Kerr rotation in saturation for the applied field along the hard (a) and easy axes (b) of the superlattice $[Fe_{52}/Cr_{17}]_9^{ET}$. The line in (b) is a calculation, making use of Eq. (1) as detailed in the text.

where M is the magnetization and M_S is the magnetization in saturation. Since M is proportional to the Kerr rotation measured by MOKE, this transformation allows for a comparison of the MOKE and PNR data. Nonetheless, this expression is not exact for the case of MOKE due to optical effects. For example it neglects the fact that due to the limited penetration of the light into the sample the individual layers may not contribute equally to the measured Kerr rotation. Even so, comparison of Figs. 14(b) and 15(b) yields a good overall agreement of all features.

Therefore, the microscopic spin structure, as directly observed by PNR with polarization analysis, can be correlated well with the macroscopic magnetic properties measured by MOKE. Since in the longitudinal geometry MOKE only measures a signal which is proportional to the resulting magnetic moment along the applied field direction, any conclusions about the microscopic magnetization profile from such MOKE data alone are not unique. This is why the combination of PNR and MOKE is very powerful in the determination of such magnetization profiles.

The MOKE hysteresis curve was also measured along the hard axis in order to compare with the corresponding PNR data. In Fig. 15(a) the MOKE curve is shown. It does not show an abrupt change in slope as for the easy axis curve. From its form one would conjecture that below saturation, with decreasing field, φ_c gradually increases from 0° to the ground state in remanence. This is exactly the behavior found by PNR. Below saturation the half-order SF peaks slowly evolve upon lowering the field, leading to the maximum intensity shown in Fig. 12. No NSF half-order peaks, which would indicate any turning process, are observed in the whole field range.

Finally it should be mentioned that no evidence for any spiral structure in any of the investigated samples has been found as predicted for multilayer structures by Rührig *et al.*[23] This is most probably due to the fact that all measurements reported here were performed after initial saturation. Trials to induce a spiral structure by another magnetization procedure have not been successful so far. As demonstrated in Ref. 63 a spiral structure would have led to a completely different PNR spectrum. For a spiral periodicity of 4Λ—a natural one for a turn angle of 90°—magnetic superlattice peaks are expected at the positions $(1/4)Q_1$ and $(3/4)Q_1$.

B. Collinear coupling

Next we demonstrate the effect of the growth temperature on the magnetic properties. In Fig. 16 the PNR results from the sample $[Fe_{52}/Cr_{17}]_5^{RT}$ are shown as obtained near remanence. In Fig. 17 the corresponding MOKE hysteresis curve is shown. The sample has the same Cr interlayer thicknesses

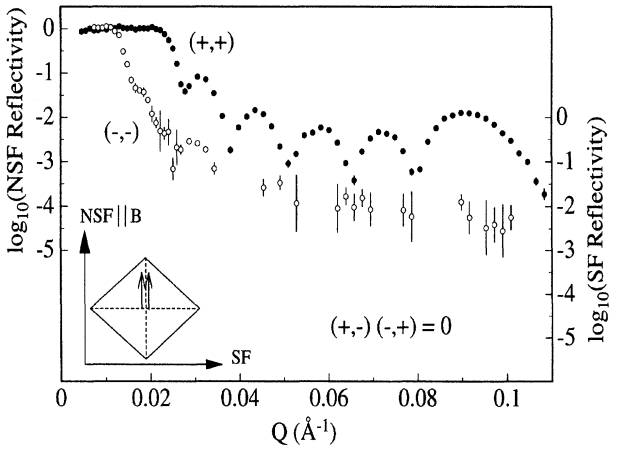

FIG. 16. PNR data of the superlattice $[Fe_{52}/Cr_{17}]_5^{RT}$ measured in $B_{GF}=17$ G parallel to an easy axis after initial saturation. SF scattering was not detected in this case.

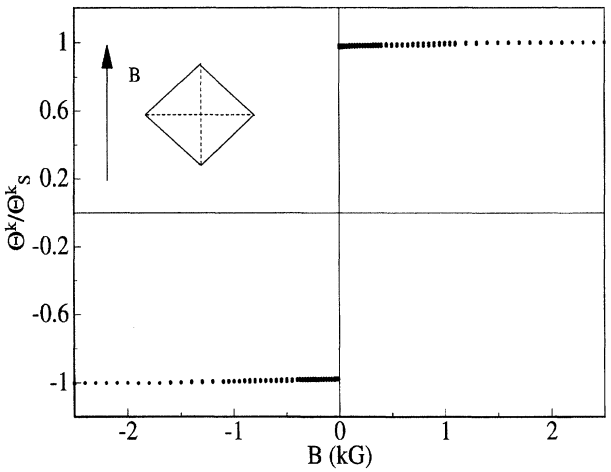

FIG. 17. Easy axis MOKE hysteresis curve of the superlattice $[Fe_{52}/Cr_{17}]_5^{RT}$.

as the one from which the spectra of Figs. 10, 13, and 15(b) originate. In all cases the data were taken with an equivalent sample orientation, i.e., with the field along the easy axis. Strikingly, the sample $[Fe_{52}/Cr_{17}]_5^{RT}$ shows a completely ferromagnetic, i.e., collinear behavior. This follows from the absence of any half-order peak in the PNR data and from the form of the MOKE curve. It should be pointed out that with the methods used here it is not possible to determine the coupling strength, since zero and strong FM coupling lead to the same PNR and MOKE spectra. The FM-like coupling behavior is in marked contrast to the noncollinear magnetization profile which was observed for the sample $[Fe_{52}/Cr_{17}]_9^{ET}$. The difference cannot be accounted for by the different number of bilayers since a noncollinear magnetization profile has also been observed for a sample of composition $[Fe_{52}/Cr_{17}]_5^{ET}$. Therefore, the growth temperature is responsible for the drastic difference in the magnetic properties and not the layer number. In the following we discuss the results in the framework of the existing theories listed in Sec. I.

V. DISCUSSION

A. Influence of the growth temperature on the exchange coupling

The results on a distinct correlation between the growth temperature and the structural properties of the sample's interfaces have been presented in Sec. III above. For growth at RT a much shorter lateral length scale l of constant Cr interlayer thickness was found than for growth at 250° (ET). In the following we demonstrate how this finding explains the differences of the magnetic properties of the RT and ET samples.

The short length scale thickness fluctuation in the RT samples will prevent the existence of a well defined Cr interlayer thickness over much more than a few atomic distances. However, a well defined interlayer thickness is required to be able to observe an oscillation of the exchange coupling with a period as small as 2 ML. Thus our result explains the suppression of the 2 ML oscillation period inherent to Cr which was observed for wedged Fe/Cr/Fe(001) trilayers[6,49] grown in the same way as the superlattices used in this study. Furthermore, following the fluctuation and the proximity magnetism models introduced in Sec. I B, the weak noncollinear contribution to the coupling in our RT sample and the wedged trilayers can be explained by the small l. On the other hand, the longer range Cr-thickness fluctuation in the ET trilayers appears to lead to a sufficiently well defined interlayer thickness over large enough length scales, allowing for the 2 ML oscillation to occur in these samples.[49] Furthermore, consistent with Slonczewski's fluctuation and proximity magnetism models, the observed large l can also explain the occurrence of an additional strong noncollinear contribution to the coupling in our ET superlattices and the ET trilayers.[49,50] In the following we will discuss these models in more detail.

B. Modeling of the exchange coupling

Within the picture of bilinear and biquadratic coupling [Eq. (1)] the observation of a coupling angle of 50° near remanence in the samples grown at 250 °C can intuitively be understood as a superposition of a large negative J^{BQ} leading to $\varphi_c = 90°$ and a large positive J^{BL} leading to FM coupling ($\varphi_c = 0°$). To calculate φ_c as a function of J^{BL}, J^{BQ}, and external field, the sum of the contributions from the two kinds of interlayer coupling between all neighboring layers in the multilayer, from the cubic magnetocrystalline in-plane anisotropy K_1 and from the external field to the energy density has to be minimized.[23] Alternatively, Eq. (1) can be replaced by Eq. (2) in the energy density, introducing Slonczewski's recent proximity magnetism model. The minimization is done numerically as a function of applied field, yielding all orientations $\varphi(B)^{(n)}$, where $n = 1,2,\ldots$ denotes one of the magnetic layers. As mentioned above, for lower fields the $\varphi(B)^{(n)}$ can be grouped into $\varphi_1(B)$ and $\varphi_2(B)$, as defined above for Eq. (5). However, at higher fields the calculations show that the two outermost layers behave differently from the inner ones because they are only coupled to one neighboring layer. This induces the disorder which is noted in the PNR spectra as a broadening of the half-order peaks. Such calculations have been used to quantitatively compare the measured data with the proposed models of a noncollinear coupling. For easier presentation of the data, normalized magnetization curves $M(B)/M_S$ are shown in Fig. (14)(b). These were obtained in analogy to Eq. (6) from the calculated $\varphi_1(B)$ and $\varphi_2(B)$ or $\varphi(B)^{(n)}$. It should be pointed out, however, that of course we directly compared the measured and calculated $\varphi(B)^{(n)}$ and not only the resulting magnetizations.

The magnitude of the magnetocrystalline cubic in-plane anisotropy K_1 strongly influences the onset of the in-plane turning process described above in the discussion of Fig. 14. However, the calculations show that its influence on φ_c near remanence is negligible. For the calculations $K_1 = 4.8 \times 10^4$ J/m^3 was used consistent with MOKE and FMR (Ref. 84) results on the sample $[Fe_{52}/Cr_{17}]_9^{ET}$.

C. Bilinear-biquadratic exchange energy

First we discuss the bilinear-biquadratic exchange energy [Eq. (1)]. In Fig. 14(b) a calculated magnetization curve (triangles) is shown with $J^{BL}=0$ and $J^{BQ}=-0.5$ mJ/m^2. The latter was chosen such that the coupling angle agreed with the PNR data at 3.9 kG. Since this PNR spectrum is the one which yields the smallest nonzero φ_c it is a good measure for the approach to saturation and the magnitude of the saturation field. The choice of coupling parameters corresponds to purely biquadratic coupling with $\varphi_c=90°$ for $B=0$ with the layer magnetizations aligned along the easy axes. Clearly, this curve completely contradicts both the measured PNR and MOKE data. In particular, the anisotropy induced change in slope due to the in-plane turning process occurs at much too high field values. Therefore, pure biquadratic coupling is inconsistent with the measured coupling angle near remanence *and* with the observed field dependence.

On the other hand, any $J^{BL}>0$ will have the effect of an additionally superimposed FM component on the $M(B)/M_S$ curves. Furthermore, near remanence it will tend to reduce the coupling angle to values less than 90°. Reasonable agreement with the observed anisotropy induced change in slope *and* the PNR result at 3.9 kG is achieved for $J^{BL}=1$ mJ/m^2 and $J^{BQ}=-1$ mJ/m^2 [crosses in Fig. 14(b) and solid line in Fig. 15(b)]. Although this model provides qualitative agreement with the PNR and MOKE results it fails in detailed comparison.

It should be pointed out that the combined errors of the experimental data and the calculation are too small to explain the observed discrepancies between theory and experiment. For example, a generous estimate of the uncertainty of the determination of φ_c by PNR near remanence yields $\pm 4°$. In principle, the theoretical calculation is mainly influenced by the value of the magnetocrystalline in-plane anisotropy K_1 and the fitted values of J^{BL} and J^{BQ}. However, as stated above, within the uncertainty of K_1 its influence on the calculated φ_c near remanence is negligible. The fitted values of J^{BL} and J^{BQ} quoted above are a best fit to the overall $\varphi_c(H)$ behavior. They provide a coupling angle of 60° near remanence whereas the PNR data give 50°. Alternatively, if J^{BL} and J^{BQ} are chosen to fit the measured $\varphi_c=50°$ near remanence and the measured φ_c at 3.9 kG, the anisotropy induced change in slope is calculated to occur at much too small fields. To account for this a much larger anisotropy constant K_1 would have to be assumed in the calculation in contradiction to the value determined independently for the same sample by FMR. Thus, the observed discrepancy between theory and experiment cannot be explained by the uncertainties in K_1 or J^{BL} and J^{BQ} alone.

Furthermore, the approach to saturation as determined by MOKE is more gradual than predicted by theory [see Fig. 15(b)]. Such an asymptotic approach to saturation contradicts Eq. (1) which always yields a well defined saturation field. This point will be discussed in some more detail below in Sec. V D.

These discrepancies indicate that the bilinear-biquadratic coupling formalism may not properly describe the observed behavior for the present sample. The results presented here among others were the motivation for Slonczewski to propose his proximity magnetism model.[47] The comparison of this model with our data will be presented further below.

1. Collinear coupling

The result of $J^{BL}+J^{BQ}\simeq 0$ obtained for the ET sample appears to be consistent with the data on Fe/Cr(001) on GaAs (Refs. 6,49) and on Fe whiskers[8] published before for $d_{Cr}=17$ Å. In contrast to our case, the techniques employed by both groups did not allow the determination of positive J^{BL}. To our knowledge such a large positive J^{BL} has never been observed before near this Cr layer thickness.[85] It should be noted, however, that from the quantitative analysis of their SEMPA images Pierce *et al.*[31] also find a large positive J^{BL} for $d_{Cr}=17$ Å, although they cannot give an absolute value.

Inspection of the existing data of Fe/Cr(001) on GaAs substrates[6,49] shows that for the sample grown at RT with $d_{Cr}=17$ Å the bilinear coupling should be close to a maximum. However, it is about one order of magnitude smaller than for the present ET sample. Following the discussion of the influence of interface roughness on the magnitude of the bilinear coupling in Sec. I A and keeping in mind the results obtained in Sec. III it is plausible that it may be the short in-plane length scale l of constant Cr thickness in the RT grown samples which significantly reduces the observable coupling strength due to the lack of a well defined interlayer thickness. Vice versa, one can conjecture that the absence of such short length scale roughness in the ET sample explains the much stronger bilinear coupling.

The RT sample $[Fe_{52}/Cr_{17}]_5^{RT}$ shows completely ferromagnetic behavior, as expected from the existing data.[6,49] However, as outlined above, a determination of the coupling strength was not possible with the available methods. Apparently, it is the short length scale Cr thickness fluctuation which suppresses the otherwise much more significant noncollinear coupling contribution.

2. Noncollinear coupling

The biquadratic coupling in the ET sample is stronger than ever observed before in the thickness regime investigated here. More important, the biquadratic coupling constant was found to be of the same magnitude as the bilinear one. So far this had been observed only for very small J^{BL}, near the zero transitions of the oscillatory bilinear coupling constant.[23,31] Here we find for the first time the coexistence of a very large positive J^{BL} with a $|J^{BQ}|$ of the same magnitude. In the following we want to discuss our results in the framework of the fluctuation and the proximity magnetism models. These currently are the only possible candidates for the understanding of noncollinear coupling in Fe/Cr(001).

The fluctuation model requires the presence of long-range interlayer thickness fluctuations in combination with a 2 ML oscillation in the bilinear coupling to explain the biquadratic coupling in the samples investigated. Thus, keeping in mind the discussion of Sec. V A, the fluctuation mechanism appears to be a prime candidate for the explanation of the observed properties. However, a contradiction arises when our results are compared with those obtained for Fe/Cr(001) on Fe whiskers[8,31] within the fluctuation model. $|J^{BQ}|$ should increase with l. According to a recent numerical computation[37] of the fluctuation model, an in-plane terrace

length of up to 1250 Å appears to be feasible. Since for the whisker experiments larger l values are obtained than in our case, $|J^{BQ}|$ should also be larger. However, smaller $|J^{BQ}|$ values are found on an absolute[8] and on a relative scale[31] for samples grown on Fe whiskers.

The three remaining biquadratic coupling mechanisms listed in Sec. I B, the intrinsic, the loose spin, and the dipole mechanisms, are much too weak to account for the measured coupling strengths. Therefore, they can only contribute in a minor way to the coupling.

D. Proximity magnetism

The most recently suggested mechanism for noncollinear coupling is Cr specific. It was introduced in Sec. I B above. To check Eq. (2) against the measured data, equivalent fits as for the bilinear-biquadratic exchange energy [Eq. (1)] have been performed. The result for $J_+ = 5$ mJ/m^2 and $J_- = 2$ mJ/m^2 is plotted in Fig. 14(b) as a solid line. Again the data are reproduced qualitatively quite well, but the quantitative agreement is not very good. For example, it was not possible to reproduce the onset of the anisotropy induced in-plane turning process around 300 G in agreement with the data without sacrificing the known $\varphi_c(B)$ determined in detail by PNR.

An important feature of Eq. (2) is, however, the description of a very gradual, i.e., asymptotic, approach to saturation. Equation (1) does not contain this feature. It always yields a well defined saturation field. The discrepancy between the MOKE data and Eq. (1) is evident from Fig. 15(b). The calculated curve approaches saturation around 4 kG nonasymptotically as a straight line and abruptly changes slope at the point of saturation [also see the equivalent calculation depicted by the crosses in Fig. 14(b)]. Such an abrupt saturation would have been detected within the high angular resolution of our MOKE apparatus. Instead, the MOKE data approach saturation not as a straight line but in an asymptotic way. Since PNR cannot distinguish $\varphi_c \leq 5°$ (see Sec. IV A 3) it cannot measure this asymptotic approach to saturation. The saturation field determined by MOKE even is somewhat higher than 4 kG. However, the assumption of coupling parameters large enough to reproduce a much larger saturation field would have led to contradictions with the MOKE and PNR data in the low field region. Thus the measured asymptotic approach appears to be inconsistent with the bilinear-biquadratric exchange energy [Eq. (1)] for the present system. On the other hand, the experimental observations qualitatively coincide with the behavior predicted by Eq. (2), providing evidence for proximity magnetism in the sample.

Furthermore, the differences between the data presented here and those obtained for Fe whisker substrates can be explained in the framework of the proximity magnetism model. Keeping in mind that the maximum l, for which the proximity magnetism model applies, is about 100 Å, we conclude from our x-ray data that the noncollinear coupling in our sample may be significantly affected by proximity magnetism. For the Fe whisker samples, on the other hand, l is much larger than 100 Å, excluding any major effect of proximity magnetism. In this case the comparatively weak noncollinear coupling could be explained by the fluctuation mechanism.[31]

Thus we find evidence for a significant contribution of proximity magnetism to the coupling properties of Fe/Cr with Cr thickness fluctuations on an intermediate length scale. The details of the exchange energy for such systems, however, are not yet well understood.

VI. CONCLUSIONS

PNR with exit beam polarization analysis has been shown to be extremely powerful in the quantitative determination of coupling angles of noncollinearly coupled superlattices. At present no other experimental technique can provide such information. Detailed quantitative analysis of the data revealed a coupling angle which significantly deviates from the perpendicular alignment anticipated so far.

It was demonstrated how microscopic and macroscopic magnetic properties can be correlated by combining PNR and MOKE. It should be pointed out that it is the detailed knowledge of the angular magnetization variation determined by PNR which allows for a direct comparison between theory and experiment. Magnetization measurements only contain a small part of the information available with PNR.

The magnetic coupling properties and their growth temperature dependence were shown to correlate well with the sample's interface structure, suggesting the length scale of the in-plane Cr-layer thickness fluctuation l as the important parameter. As opposed to the usual surface science methods our x-ray method provided information on the *internal* interfaces. For small l we find FM or uncoupled behavior whereas an intermediate $l \approx 100$ Å induces a strong noncollinear coupling.

Surprisingly, the strength of the observed coupling was found to be larger than ever observed before in this system for the Cr thickness investigated. Furthermore, it was shown that the observed 50° coupling angle near remanence can be understood at least qualitatively either as a superposition of bilinear (FM) and equally large biquadratic (90°) coupling or within the proximity magnetism model. Both exchange energy formalisms, which we tested against our field dependent data, were found to reproduce typical features, but did not fit well quantitatively. However, our results bear strong evidence for the significance of the recently proposed proximity magnetism model in Fe/Cr for the intermediate length scale of the Cr thickness fluctuations in our samples. The asymptotic approach to saturation measured by MOKE is only reproduced by the proximity magnetism model. Proximity magnetism would also provide a natural explanation for the different behavior (stronger coupling, 50° coupling angle) of our samples as compared to others grown on Fe whiskers having a larger length scale of Cr thickness fluctuations. The fluctuation mechanism alone leads to a contradiction between our and the Fe whisker data.

More theoretical and experimental work is required to quantitatively understand the exchange energy in systems with Cr spacers. For the near future we are planning experiments designed to further investigate micromagnetic models. These will include PNR measurements of the dependence of the coupling angle on temperature and on the thickness of the Cr interlayers. Furthermore we are investigating the or

dering of the Cr spins in the interlayers with neutron scattering methods. This should allow us to correlate the Cr magnetism directly with the exchange coupling properties between the Fe layers.

ACKNOWLEDGMENTS

We want to thank J. C. Slonczewski for his interest in our work and R. Schreiber for his help with sample preparation. Furthermore, we thank A. Abromeit for his assistance with the modeling of the diffuse x-ray scattering and R. Meckenstock and D. Kurowski for the FMR measurements. We gratefully acknowledge financial support from the German Bundesministerium für Bildung, Wissenschaft, Forschung und Technologie (Grant No. ZA03BOC) and the Deutsche Forschungsgemeinschaft via Sonderforschungsbereich 166 for the work in Bochum as well as a travel grant from NATO (Grant No. CRG901064).

*Present address: Naval Research Lab., Washington, D.C. 20375-5000.

[1] C.F. Majkrzak, J.W. Cable, J. Kwo, M. Hong, D.B. McWhan, Y. Yafet, J.V. Waszczak, H. Grimm, and C. Vettier, Phys. Rev. Lett. **56**, 2700 (1986).

[2] P. Grünberg, R. Schreiber, Y. Pang, M.B. Brodsky, and H. Sowers, Phys. Rev. Lett. **57**, 2442 (1986).

[3] M.N. Baibich, J.M. Broto, A. Fert, F. Nguyen van Dau, F. Petroff, P. Etienne, G. Creuzet, A. Friederich, and J. Chazelas, Phys. Rev. Lett. **61**, 2472 (1988).

[4] G. Binasch, P. Grünberg, F. Saurenbach, and W. Zinn, Phys. Rev. B **39**, 4828 (1989).

[5] S.S.P. Parkin, N. More, and K.P. Roche, Phys. Rev. Lett. **64**, 2304 (1990).

[6] S. Demokritov, J.A. Wolf, and P. Grünberg, Europhys. Lett. **15**, 881 (1991).

[7] S.S.P. Parkin, Phys. Rev. Lett. **67**, 3598 (1991).

[8] B. Heinrich and J.F. Cochran, Adv. Phys. **42**, 523 (1993).

[9] *Ultrathin Magnetic Structures*, edited by J.A.C. Bland and B. Heinrich (Springer-Verlag, Berlin, 1994), Vols. I and II.

[10] C.F. Majkrzak, J. Kwo, M. Hong, Y. Yafet, D. Gibbs, C.L. Chien, and J. Bohr, Adv. Phys. **40**, 99 (1991).

[11] P. Bruno and C. Chappert, Phys. Rev. Lett. **67**, 1602 (1991).

[12] D.M. Edwards, J. Mathon, R.B. Muniz, and M.S. Phan, Phys. Rev. Lett. **67**, 493 (1991).

[13] R. Coehoorn, Phys. Rev. B **44**, 9331 (1991).

[14] P. Bruno and C. Chappert, Phys. Rev. B **46**, 261 (1992).

[15] M.T. Johnson, S.T. Purcell, N.W.E. McGee, R. Coehoorn, J. aan de Stegge, and W. Hoving, Phys. Rev. Lett. **68**, 2688 (1992).

[16] M.T. Johnson, R. Coehoorn, J.J. de Vries, N.W.E. McGee, J. aan de Stegge, and P.J.H. Bloemen, Phys Rev. Lett. **69**, 969 (1992).

[17] A. Schreyer, K. Bröhl, J.F. Ankner, C.F. Majkrzak, Th. Zeidler, P. Bödeker, N. Metoki, and H. Zabel, Phys. Rev. B **47**, 15 334 (1993).

[18] P. Bruno, J. Magn. Magn. Mater. **121**, 248 (1993).

[19] See Ref. 18 for a list; a number of more recent theoretical papers can be found in the same conference proceedings.

[20] M.D. Stiles, Phys. Rev. B **48**, 7238 (1993).

[21] See, for example, M. van Schilfgaarde and F. Herman, Phys. Rev. Lett. **71**, 3870 (1993).

[22] Y. Wang, P.M. Levy, and J.L. Fry, Phys. Rev. Lett. **65**, 2732 (1990).

[23] M. Rührig, R. Schäfer, A. Hubert, R. Mosler, J.A. Wolf, S. Demokritov, and P. Grünberg, Phys. Status Solidi A **125**, 635 (1991).

[24] B. Heinrich, J.F. Cochran, M. Kowalewski, J. Kirschner, Z. Celinski, A.S. Arrott, and K. Myrtle, Phys. Rev. B **44**, 9348 (1991).

[25] A. Fuss, S. Demokritov, P. Grünberg, and W. Zinn, J. Magn. Magn. Mater. **103**, L221 (1992).

[26] B. Heinrich, Z. Celinski, J.F. Cochran, A.S. Arrott, K. Myrtle, and S.T. Purcell, Phys. Rev. B **47**, 5077 (1993).

[27] Z. Celinski, B. Heinrich, and J.F. Cochran, J. Appl. Phys. **73**, 5966 (1993).

[28] J. Unguris, R.J. Cellotta, D.T. Pierce, and J.A. Stroscio, J. Appl. Phys. **73**, 5984 (1993).

[29] C.J. Gutierrez, J.J. Krebs, M.E. Filipkowski, and G.A. Prinz, J. Magn. Magn. Mater. **116**, L305 (1992).

[30] M.E. Filipkowski, C.J. Gutierrez, J.J. Krebs, and G.A. Prinz, J. Appl. Phys. **73**, 5963 (1993).

[31] D.T. Pierce, Joseph A. Stroscio, J. Unguris, and R.J. Celotta, Phys. Rev. B **49**, 14 564 (1994).

[32] J.C. Slonczewski, J. Appl. Phys. **73**, 5957 (1993).

[33] J.C. Slonczewski, Phys. Rev. Lett. **67**, 3172 (1991).

[34] J. Unguris, R.J. Cellotta, and D.T. Pierce, Phys. Rev. Lett. **67**, 140 (1991).

[35] S.T. Purcell, W. Folkerts, M.T. Johnson, N.W.E. McGee, K. Jager, J. aan de Stegge, W.B. Zeper, W. Hoving, and P. Grünberg, Phys. Rev. Lett. **67**, 903 (1991).

[36] R. Ribas and B. Dieny, Phys. Lett. A **167**, 103 (1992).

[37] R. Ribas and B. Dieny, J. Magn. Magn. Mater. **121**, 313 (1993).

[38] J. Barnaś, J. Magn. Magn. Mater. **123**, L21 (1993).

[39] J. Barnaś and P. Grünberg, J. Magn. Magn. Mater. **121**, 326 (1993).

[40] R.P. Erickson, K.B. Hathaway, and J.R. Cullen, Phys. Rev. B **47**, 2626 (1993).

[41] D.M. Edwards, J.M. Ward, and J. Mathon, J. Magn. Magn. Mater. **126**, 380 (1993).

[42] J.C. Slonczewski, J. Magn. Magn. Mater. **126**, 374 (1993).

[43] A. Fuss, J.A. Wolf, and P.A. Grünberg, Phys. Scr. **T45**, 95 (1992).

[44] M. Schäfer, S. Demokritov, S. Müller-Pfeiffer, R. Schäfer, M. Schneider, P. Grünberg, and W. Zinn, J. Appl. Phys. **77**, 6432 (1995).

[45] B. Heinrich, M. From, J.F. Cochran, M. Kowalewski, D. Atlan, Z. Celinski, and K. Myrtle, *Proceedings of the International Conference on Magnetism*, Warsaw, Poland, 1994 [J. Magn. Magn. Mater. **140-144**, 545 (1995)].

[46] S. Demokritov, E. Tsymbal, P. Grünberg, W. Zinn, and I.K. Schuller, Phys. Rev. B **49**, 720 (1994).

[47] J.C. Slonczewski, J. Magn. Magn. Mater. **150**, 13 (1995).

[48] J. Unguris, R.J. Celotta, and D.T. Pierce, Phys. Rev. Lett. **69**, 1125 (1992).

[49] J.A. Wolf, Q. Leng, R. Schreiber, P.A. Grünberg, and W. Zinn, J. Magn. Magn. Mater. **121**, 253 (1993).

[50] J.A. Wolf, Ph.D. thesis, Universtät Köln, 1993 (Berichte des Forschungszentrums Jülich **2743**).

[51] A. Barthélémy, A. Fert, M.N. Baibich, S. Hadjoudj, F. Petroff, P.

Etienne, R. Cabanel, S. Lequien, F. Nguyen Van Dau, and G. Creuzet, J. Appl. Phys. **67**, 5908 (1990).

[52] N. Hosoito, S. Araki, K. Mibo, and T. Shinjo, J. Phys. Soc. Jpn. **59**, 1925 (1990).

[53] S.S.P. Parkin, A. Mansour, and G.P. Felcher, Appl. Phys. Lett. **58**, 1473 (1991).

[54] J.A.C. Bland, R.D. Bateson, N.F. Johnson, S.J. Blundell, V.S. Speriosu, S. Metin, B.A. Gurney, and J. Penfold, J. Magn. Magn. Mater. **123**, 320 (1993).

[55] N. Hosoito, K. Mibu, S. Araki, T. Shinjo, S. Itoh, and Y. Endoh, J. Phys. Soc. Jpn. **61**, 300 (1992).

[56] K. Takanashi, Y. Obi, N. Tsuda, and H. Fujimori, J. Phys. Soc. Jpn. **61**, 4148 (1992).

[57] M. Loewenhaupt, W. Hahn, Y.Y. Huang, G.P. Felcher, and S.S.P. Parkin, J. Magn. Magn. Mater. **121**, 173 (1993).

[58] N. Hosoito, K. Mibu, T. Ono, T. Shinjo, and Y. Endoh, J. Magn. Magn. Mater. **126**, 255 (1993).

[59] M. Takeda, H. Yasuda, T. Watanabe, K. Yamada, Y. Endoh, A. Kamijo, and J. Mizuki, J. Magn. Magn. Mater. **126**, 355 (1993).

[60] A. Schreyer, J.F. Ankner, H. Zabel, M. Schäfer, C.F. Majkrzak, and P. Grünberg, *Proceedings of the 3rd International Conference on Surface X-Ray and Neutron Scattering*, Dubna, 1993 [Physica B **198**, 173 (1994)].

[61] J.F. Ankner, A. Schreyer, Th. Zeidler, C.F. Majkrzak, H. Zabel, J.A. Wolf, and P. Grünberg, in *Magnetic Ultrathin Films, Multilayers and Surfaces*, edited by C. Chappert, R. Clarke, R.F.C. Farrow, P. Grünberg, W.J.M. de Jonge, B.T. Jonker, Kannan M. Krishnan, and Shigeru Tsunashima, MRS Symposia Proceedings No. 313 (Materials Research Society, Pittsburgh, 1993), p. 761.

[62] A. Schreyer, J.F. Ankner, M. Schäfer, Th. Zeidler, H. Zabel, C.F. Majkrzak, and P. Grünberg, *Proceedings of the 14th International Colloquium on Magnetic Films and Surfaces*, Düsseldorf, Germany, 1994 [J. Magn. Magn. Mater. **148**, 189 (1995)].

[63] H. Zabel, *Proceedings of the 3rd International Conference on Surface X-Ray and Neutron Scattering*, Dubna, 1993 [Physica B **198**, 156 (1994)].

[64] D.E. Savage, J. Kleiner, N. Schimke, Y.-H. Pang, T. Jankowski, J. Jacobs, R. Kariotis, and M.G. Lagally, J. Appl. Phys. **69**, 1411 (1991).

[65] J.F. Ankner, in *Surface X-Ray and Neutron Scattering*, edited by H. Zabel and I.K. Robinson, Springer Proceedings in Physics Vol. 61 (Springer, Berlin, 1992), p. 105.

[66] J.F. Ankner and C.F. Majkrzak, *Neutron Optical Devices and Applications*, Proc. SPIE Vol. 1738 (SPIE, Bellingham, WA, 1992), p. 260.

[67] See, for example, *Surface X-Ray and Neutron Scattering*, edited by H. Zabel and I.K. Robinson, Springer Proceedings in Physics Vol. 61 (Springer, Berlin, 1992).

[68] G.P. Felcher, R.O. Hilleke, R.K. Crawford, J. Haumann, R. Kleb, and G. Ostrowski, Rev. Sci. Instrum. **58**, 609 (1987).

[69] C.F. Majkrzak, Physica B **156&157**, 619 (1989).

[70] C.F. Majkrzak, Physica B **173**, 75 (1991).

[71] A. Schreyer, Th. Zeidler, Ch. Morawe, N. Metoki, H. Zabel, J.F. Ankner, and C.F. Majkrzak, J. Appl. Phys. **73**, 7616 (1993).

[72] G.P. Felcher, Physica B **192**, 137 (1993).

[73] C.F. Majkrzak, in *Handbook of Neutron Scattering*, edited by W. Gläser (Springer-Verlag, Heidelberg, in press).

[74] C.F. Majkrzak, *Proceedings of the 4th International Conference on Surface X-Ray and Neutron Scattering*, Lake Geneva, Wisconsin, 1995 [Physica B (to be published)].

[75] A. Schreyer, Ph.D. thesis, Ruhr-Universität Bochum, 1994 [available via the WWW at http://www.ep4.ruhr-uni-bochum.de/people/as].

[76] See, for example; S.D. Bader, J. Magn. Magn. Mater. **100**, 440 (1991).

[77] N. Metoki, Th. Zeidler, A. Stierle, K. Bröhl, and H. Zabel, J. Magn. Magn. Mater. **118**, 57 (1993).

[78] A.P. Payne and B.M. Clemens, Phys. Rev. B **47**, 2289 (1993).

[79] V. Holý and T. Baumbach, Phys. Rev. B **49**, 10 668 (1994); J.-P. Schlomka, M. Tolan, L. Schwalowsky, O.H. Seeck, J. Stettner, and W. Press, Phys. Rev. B **51**, 2311 (1995). In the first paper a multilayer with 20 periods was considered, but the model was restricted to one in-plane correlation length equal for all interfaces. In the present case we deal with ξ_u and ξ_c. In the second paper the number of interfaces was much smaller than considered here.

[80] D.E. Bürgler, C.M. Schmidt, T.M. Schaub, and H.J. Güntherodt (unpublished).

[81] J.A. Stroscio, D.T. Pierce, and R.A. Dragoset, Phys. Rev. Lett. **70**, 3615 (1993).

[82] P. Bödeker, A. Abromeit, K. Bröhl, P. Sonntag, N. Metoki, and H. Zabel, Phys. Rev. B **47**, 2353 (1993).

[83] H. Rauch, in *Neutron Interferometry*, edited by U. Bonse and H. Rauch (Clarendon Press, Oxford, 1979), p. 174.

[84] D. Kurowski and R. Meckenstock (private communication).

[85] A quite recent comparative discussion of the available results can be found, e.g., in the review by Heinrich and Cochran (Ref. 8).

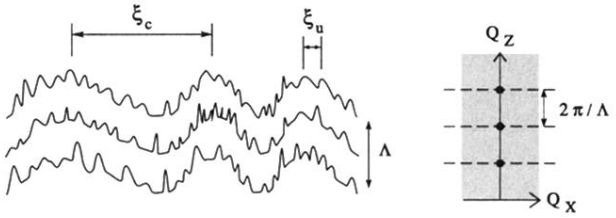

FIG. 6. Schematic cross-sectional view in real space (left) and the intensity distribution in Q space (right) for a multilayer with vertically correlated and uncorrelated roughness components which are characterized by the in-plane correlation lengths ξ_c and ξ_u, respectively. The correlated roughness leads to maxima in the off-specular (diffuse) intensity along Q_z (dashed lines) whereas the uncorrelated roughness causes diffuse intensity without such structure. Thus ξ_c can be determined using Q_x scans along the maxima in Q_z (dashed lines). ξ_u is obtained from Q_x scans between these maxima. For the angular range of interest the Q_x scans can be approximated very well by the rocking curves depicted in Fig. 1(b).